Chapter 1
Geochemistry of Cold Hydrocarbon Seeps: An Overview

J. Kirk Cochran, Neil H. Landman, Michał Jakubowicz, Jamie Brezina, Jone Naujokaityte, Ana Rashkova, Matthew P. Garb, and Neal L. Larson

J. K. Cochran (✉)
School of Marine and Atmospheric Sciences, Stony Brook University, Stony Brook, NY, USA

Department of Invertebrate Paleontology, American Museum of Natural History, New York, NY, USA
e-mail: kirk.cochran@stonybrook.edu

N. H. Landman · A. Rashkova
Department of Invertebrate Paleontology, American Museum of Natural History, New York, NY, USA
e-mail: landman@amnh.org; arashkova@amnh.org

M. Jakubowicz
Isotope Research Unit, Adam Mickiewicz University, Poznań, Poland
e-mail: mjakub@amu.edu.pl

J. Brezina
Department of Mining Engineering and Management, South Dakota School of Mines and Technology, Rapid City, SD, USA

J. Naujokaityte
Department of Earth and Planetary Sciences, University of New Mexico, Albuquerque, NM, USA
e-mail: jnaujokaityte@unm.edu

M. P. Garb
Department of Earth and Environmental Sciences, Brooklyn College, Brooklyn, NY, USA
e-mail: mgarb@brooklyn.cuny.edu

N. L. Larson
Larson Paleontology Unlimited, Keystone, SD, USA
e-mail: neal@larsonpaleo.com

A. Kaim et al. (eds.), *Ancient Hydrocarbon Seeps*, Topics in Geobiology 53,
https://doi.org/10.1007/978-3-031-05623-9_1

1.1 Introduction

Cold methane or hydrocarbon seeps have been documented throughout the Phanerozoic, with the oldest deposits dating to ~635 Ma (Bristow and Grotzinger 2013; Shields et al. 2007; Kennedy et al. 2008; Fig. 1.1). They are typically recognized by unusual carbonate concretionary deposits with isotopically low $\delta^{13}C$ signatures (<−30‰ VPDB), mineralogies ranging from Mg-calcite to aragonite, and unusual morphologies (e. g., pipes, crusts, isolated masses). The fundamental process operating at seeps is the anaerobic oxidation of methane (AOM), mediated by a consortium of anaerobic methanotrophic archaea (ANME) and sulfate-reducing bacteria (SRB; Boetius et al. 2000). This chapter explores in detail the conditions and pathways by which AOM occurs and the related co-occurring biogeochemical processes, including methanogenesis, organoclastic sulfate reduction, iron reduction, and sedimentary pyrite formation, that lead to the features observed at present-day methane seeps and aid in the interpretation of similar features at fossil seeps. As well, we discuss the application of selected isotope (C, O, Sr, Nd) and elemental systems (rare earth elements, Fe, Mn, Sr, Mg) to seep carbonates. These data provide critical information about the composition of the fluids feeding the hydrocarbon system, validation of methane-derived carbon in the system, temperature of carbonate formation, and constraints on fluid circulation.

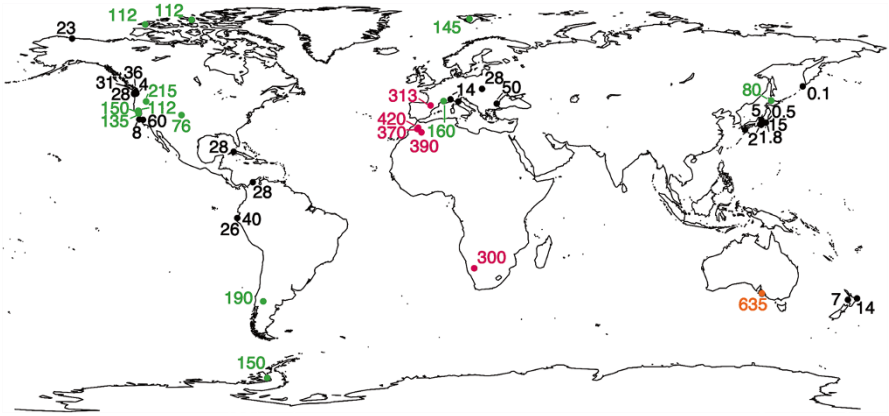

Fig. 1.1 Map of ancient methane seep locations and ages (in Ma). Precambrian cold seep carbonates lack the distinctive low $\delta^{13}C$ signatures that are characteristic of younger seeps (<200 Ma), likely due to lower seawater sulfate and higher dissolved inorganic carbon concentrations. Color coding of ages: Precambrian, *orange*; Paleozoic, *red*; Mesozoic, *green*; Cenozoic, *black*. Some dots represent multiple seeps. (Modified from Bristow and Grotzinger (2013) and reprinted with permission of the Geological Society of America. For a more complete listing of the global distribution of seeps, see Hryniewicz this volume-b)

1.2 The Redox Cascade

Microbes oxidize the carbon in organic matter (herein represented as CH_2O) in marine sediments during early diagenesis using a sequence of electron acceptors: O_2, NO_3^-, Mn^{4+} (as MnO_2), Fe^{3+} (e.g., as FeOOH), and SO_4^{2-}, in what is termed the "redox cascade." The sequence is determined by the standard state free energy change associated with each reaction, with aerobic oxidation producing the greatest energy yield (Berner 1980). An important reaction in this sequence is the organoclastic reduction of pore water sulfate by sulfate-reducing bacteria (e.g., *Desulfovibrio* sp.) to produce bicarbonate ions and hydrogen sulfide (Fig. 1.2):

$$SO_4^{2-} + 2CH_2O \rightarrow 2HCO_3^- + H_2S \tag{1.1}$$

Sulfate reduction via Reaction 1.1 occurs in the upper decimeters to meters of the sediment, depending on the amount and lability of organic matter in the sediment, as well as the sulfate concentration. Figure 1.3a shows how the depth of sulfate reduction varies globally. Organic-rich coastal and ocean margin sediments show depletion of sulfate at shallower depths in the sediment column relative to organic-poor deep-sea sediments.

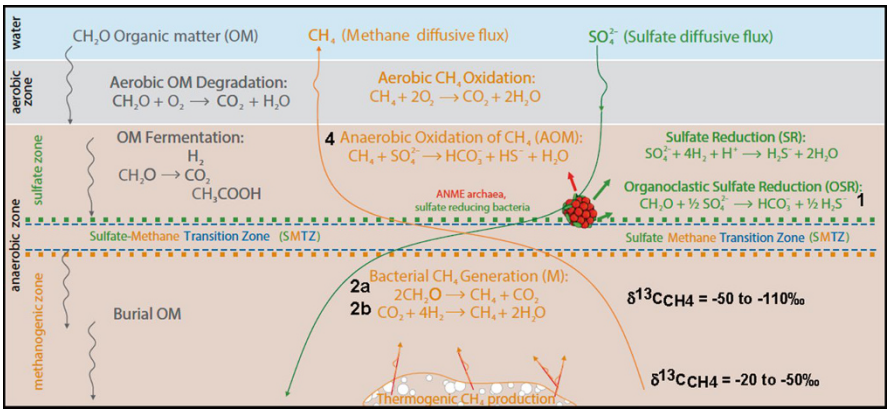

Fig. 1.2 Schematic diagram showing microbially mediated processes of organic matter transformation in marine sediments. Methane is produced at depth in the sediments (biogenically via Reactions 1.2a, 1.2b, and 1.2c) and 1.3 or thermogenically), while organoclastic sulfate reduction (Reaction 1.1) is a major pathway by which organic matter is oxidized in the "sulfate zone." Methane diffuses upward (orange arrow), encounters residual sulfate in the "sulfate-methane transition zone" (SMTZ), and promotes anaerobic oxidation of methane (AOM) (Reaction 1.4). Production of bicarbonate via AOM drives precipitation of authigenic seep carbonates (text Reaction 1.5, not shown in figure). Methane that escapes oxidation via AOM can be oxidized aerobically in the aerobic zone or in overlying oxic waters. Bold numbers refer to Reactions (1.x) in text. (Modified from Matveeva et al. 2015; Used under Creative Commons License; https://creativecommons.org/licenses/by/4.0/)

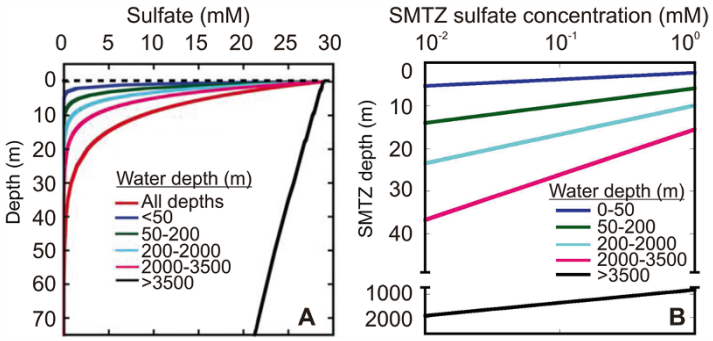

Fig. 1.3 (**a**) Pore water sulfate vs. depth in sediment deposited at different depths of water. The variation reflects the rate of sulfate reduction, in turn a function of the availability of organic matter (OM) and alternate electron acceptors that drive OM oxidation. (**b**) Average depth (m) of the sulfate-methane transition zone (SMTZ) as a function of SMTZ sulfate concentrations (in mM). In shallow-water, organic-rich sediments, the SMTZ is located close to the sediment-water interface, while in deeper water, it may be 10s of meters below. (Reprinted from Bowles et al. 2014 with permission from AAAS)

As sulfate is depleted in sediment pore water, a final step in organic matter decomposition involves the production of methane via a net reaction that is effectively the disproportionation of carbon in organic matter (represented here as CH_2O) by methanogenic archaea:

$$2CH_2O \rightarrow CO_2 + CH_4 \tag{1.2a}$$

Reaction 1.2a involves the coupling of organic matter oxidation to CO_2 and hydrogen in fermentation with the reaction of CO_2 with H_2 to yield methane (Berner 1980; Fig. 1.2):

$$2CH_2O + 2H_2O \rightarrow 2CO_2 + 4H_2 \tag{1.2b}$$

$$4H_2 + CO_2 \rightarrow CH_4 + 2H_2O \tag{1.2c}$$

An alternate pathway for methane production involves acetate disproportionation (Sansone and Martens 1981; Ferry 1992; Burdige 2006):

$$CH_3COOH \rightarrow CO_2 + CH_4 \tag{1.3}$$

Methane produced by Reactions 1.2a, b, c and 1.3 is termed "biogenic" to differentiate it from the production of "thermogenic" methane from deeply buried organic matter subjected to elevated temperatures and pressures (Fig. 1.2). Reactions 1.2 and 1.3 involve a large fractionation in stable carbon isotopes between marine organic matter ($\delta^{13}C \sim -20‰$) and the products CO_2 and CH_4. The methane so produced has a carbon isotope composition that is lower than that of the organic matter ($\delta^{13}C \sim -20$ to $-50‰$ for thermogenic methane and -50 to $-110‰$ for biogenic methane; Whiticar 1999), while the CO_2 has $\delta^{13}C$ values ranging from +5 to +24‰.

Under certain combinations of pressure (elevated) and temperature (low), methane can become incorporated into methane hydrates, a combination of water and methane molecules in a solid cage-like structure (Matsumoto 2001; Bohrmann and Torres 2006). Methane hydrates are stable under conditions of low temperature and high pressure, such as encountered in sediments accumulating in several hundred meters of water or deeper, as well as at depth in deep-sea sediments (Matsumoto 2001; Bohrmann and Torres 2006). Outside of the zone of gas hydrate stability (e.g., in shallow shelf sediments), methane is not present associated with hydrates and is dissolved in the pore water or perhaps is exsolved as gas bubbles.

1.3 Methane Oxidation

The upward migration of dissolved methane in sediments by advective or diffusive transport makes it susceptible to oxidation. This can be carried out aerobically if methane diffuses into the oxic zone of the sediments (Fig. 1.2), or anaerobically by the process of anaerobic methane oxidation (AOM), which involves a symbiotic consortium between several clades of anaerobic methanotrophic archaea (ANME; ANME-1, ANME-2, and ANME-3) and sulfate-reducing bacteria (Knittel and Boetius 2009) via the reaction:

$$CH_4 + SO_4^{2-} \rightarrow HCO_3^- + HS^- + H_2O \quad (1.4)$$

As noted above, the methane oxidized via AOM has a low $\delta^{13}C$ value, and this is imprinted on the produced HCO_3^- and, thus, on the dissolved inorganic carbon (DIC) reservoir of the pore fluids. Modern and ancient seep carbonates typically show low $\delta^{13}C$ values as a consequence of precipitation from this ^{12}C-enriched DIC reservoir (see Sect. 1.6.1).

Sulfate is a necessary reactant for AOM via Reaction 1.4, and given the independent organoclastic reduction of sulfate to oxidize organic matter (Reaction 1.1; Figs. 1.2 and 1.3a), AOM takes place in a region termed the "sulfate-methane transition zone" (SMTZ; Fig. 1.2), i.e., the depth region in the sediment column in which both sulfate and methane co-exist. For seeps occurring in relatively shallow water, this is likely to be close (within a few meters) to the sediment-water interface; conversely, sediments in deeper water have deeper SMTZ depths in the sediment (Fig. 1.3b; Bowles et al. 2014). This is due to lower concentrations of labile organic matter and slower rates of methane production and sulfate reduction. The depth and thickness of the SMTZ also depend on the transport mechanisms for sulfate and methane in the pore fluid. Figures 1.2 and 1.3 depict the situation when molecular diffusion controls the transport of these chemical species – downward diffusion (+ reaction) of sulfate from its source in the overlying water and upward diffusion (+ reaction) of methane produced at depth in the sediment. Advective (or effusive) transport of pore fluid in the sediment may also occur, for example, through extensive bio-irrigation of burrows by infauna. Tectonic activity such as faulting (Sample

et al. 1993) or sediment compaction and dewatering at subduction zones (Han et al. 2004) may also facilitate transport of pore fluids through the deposit and displace the SMTZ upward toward the sediment-water interface.

In addition to AOM via a consortium of ANME and sulfate-reducing bacteria, several alternative pathways of microbial AOM have been documented (Joye 2012). These include AOM via reduction of manganese (or iron) oxide (Beal et al. 2009), bacterial AOM by disproportionation of nitrite (NO_2^-; Ettwig et al. 2010), and AOM by ANME-2 accompanied by disproportionation of sulfate to disulfide (Milucka et al. 2012). The significance of the latter process is that it can be carried out by methanotrophic archaea alone, without the associated bacteria. However, most AOM in marine sediments takes place via Reaction 1.4 with the consortium of methanotrophic archaea and sulfate-reducing bacteria.

The concentration of seawater sulfate has varied with time over Earth history (Planavsky et al. 2012), and the dependence of AOM on sulfate may in part account for the abundance of seeps over time (Bristow and Grotzinger 2013). In particular, seawater sulfate concentrations have been >5 mM in the last ~350 Ma, and seep abundance is more evident over this time (Planavsky et al. 2012). Indeed, Kiel (2015) has proposed that variable seawater sulfate concentrations are responsible for the evolution of deep-sea seep ecosystems over the past 150 Ma. This was a

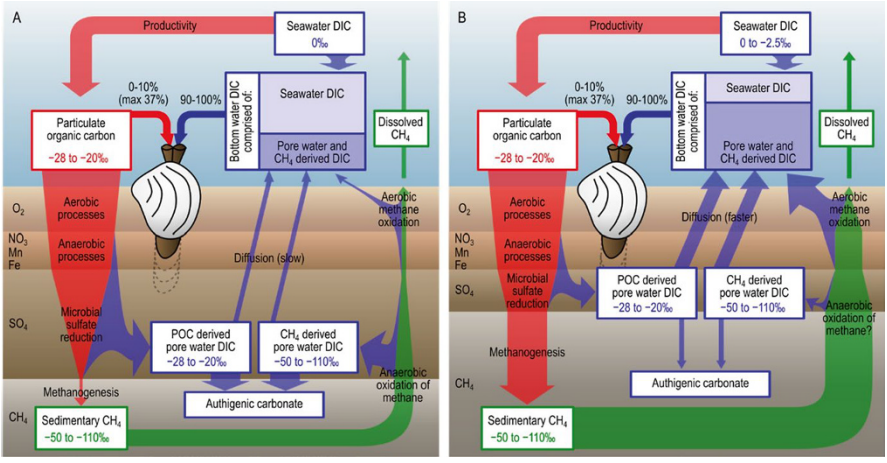

Fig. 1.4 Conceptual model of the sedimentary carbon cycle under high and low sulfate conditions. Conceptual diagram of fluxes of POC (red), DIC (blue), and methane (green) under (**a**) modern high sulfate conditions and (**b**) Cretaceous lower sulfate conditions. Thickness of arrows represents relative strength of flux to each reservoir (not to scale). Depth scales are arbitrary; bottom-water reservoir refers to the benthic boundary layer sampled by bivalves and is likely to be only 5–10 cm in depth. The depth of the sulfate reduction zone is variable in modern marine sediments, depending on factors such as diffusion and bioturbation (see Fig. 1.3). Bivalves, living on or in the sediment, incorporate carbon from both the DIC (90–100%), and metabolic carbon (0–10%) reservoirs into their shells. Reactions corresponding to the processes illustrated are shown in Fig. 1.2 and given in the text. (From Hall et al. 2018; used under Creative Commons License, https://creativecommons.org/licenses/by/4.0/)

period over which seawater sulfate concentrations more than doubled from ~10 mM to the present value of 28 mM. Lower concentrations of sulfate in the past (e.g., Cretaceous) may have shifted the redox cascade in favor of methanogenesis and possibly allowed the SMTZ to move closer to the sediment-water interface (Hall et al. 2018). Figure 1.4 shows this effect, through a comparison of two seep systems with different seawater sulfate concentrations representing the modern and Cretaceous ocean (Hall et al. 2018).

1.4 Seep Carbonate Formation

A consequence of AOM is an increase in the dissolved inorganic carbon reservoir (through production of HCO_3^-) leading to supersaturation with respect to $CaCO_3$ and the precipitation of authigenic carbonates:

$$2HCO_3^- + Ca^{2+} \rightarrow CaCO_3 + CO_2 + H_2O \quad (1.5)$$

The carbonate minerals formed via Reaction 1.5 include microcrystalline high-Mg (>5% Mg) calcite, as well as dolomite, aragonite, and iron-rich carbonates (Stakes et al. 1999; Campbell et al. 2002; Greinert et al. 2002; Luff and Wallmann 2003; Mazzini et al. 2004; Reitner et al. 2005; Naehr et al. 2007; Pierre et al. 2014; Hryniewicz this volume-a). Transformations during burial and later in diagenesis can yield low-Mg calcite (Joseph et al. 2013).

Morphologies of the precipitated carbonates vary widely and include crusts (Luff et al. 2004), strata-bound carbonate layers (Natalicchio et al. 2012), small rod- and dumbbell-shaped concretions (Reitner et al. 2005), tubes and pipes (Cochran et al. 2015; Cavagna et al. 2015), and massive limestones (Michaelis et al. 2002; Reitner et al. 2005; Wiese et al. 2015; Smrzka et al. 2017; Miyajima et al. 2018; Hryniewicz this volume-a). These variations reflect the nature of methane transport through the sediment (diffusive vs. advective transport), rates of transport, rates of AOM, position of the SMTZ, and the temporal evolution of a seep system (Stakes et al. 1999; Naehr et al. 2007; Luff and Wallmann 2003; Luff et al. 2004; Pierre et al. 2014; Miyajima et al. 2018).

1.5 Iron and Sulfur Cycling at Seeps

As noted above, Fe^{3+} is used as an electron acceptor utilized by bacteria to oxidize organic matter during early diagenesis (Berner 1980):

$$CH_2O + 7H^+ + 4FeOOH \rightarrow 4Fe^{2+} + HCO_3^- + 6H_2O \quad (1.6)$$

As a consequence, dissolved hydrogen sulfide and reduced Fe^{2+} (produced via Reactions 1.1, 1.4, and 1.6) can react to form iron monosulfides and, subsequently, phases such as pyrite (FeS_2) and greigite (Fe_3S_4). Indeed, if Fe reduction and AOM occur in close proximity in the sediment column, Peckmann et al. (2003) and Peckmann and Thiel (2004) have proposed that Reactions 1.4 and 1.6 can be coupled:

$$4CH_4 + CH_2O + 4SO_4^{2-} + 4FeOOH + 3H^+ \rightarrow 5HCO_3^- + 4FeS + 10H_2O \quad (1.7)$$

The combined reaction promotes carbonate precipitation (via Reaction 1.5) as well as FeS formation and may help explain the presence of iron sulfides within carbonate nodules in some seep deposits (e.g., Peckmann and Thiel 2004).

AOM is by definition an anaerobic process and, thus, not one that occurs in oxic water columns above seep sites. The formation of carbonates at most modern cold seeps is, thus, confined to the sediments, although often near the sediment-water interface. Carbonate build-ups (i.e., chemoherms; Aharon 1994) in the water column are mostly limited to anoxic basins such as the Black Sea (Michaelis et al. 2002). Where carbonate crusts, pinnacles, or chimneys are presently observed in oxic water columns, as at the Amon mud volcano on the Nile deep-sea fan in the Mediterranean, they are hypothesized to have formed at a time when the bottom water was suboxic or anoxic (Bayon et al. 2013) or, as in the Adriatic Sea, at an earlier time with subsequent exhumation (Angeletti et al. 2015).

An alternate mechanism for the development of chemoherms above the sediment-water interface in oxic waters has been proposed by Teichert et al. (2005). Their observations of such deposits on Hydrate Ridge on the Cascadia margin show the presence of sulfur-oxidizing bacterial mats (of the genus *Beggiatoa*) covering the deposit. The intense production of hydrogen sulfide via AOM, as well as from organoclastic sulfate reduction, provides a source of sulfide for such bacteria. Indeed, *Beggiatoa* sp. can use dissolved O_2 to oxidize sulfide and form organic matter (Jørgensen and Nelson 2004; Schwedt et al. 2012) as:

$$4H_2S + 7O_2 + CO_2 + H_2O \rightarrow 4SO_4^{2-} + CH_2O + 8H^+ \quad (1.8)$$

Although Reaction 1.8 produces acid (H^+) that might inhibit AOM-produced carbonate precipitation (or indeed dissolve carbonates so produced; Peckmann et al. 2004), Teichert et al. (2005) proposed that *Beggiatoa* mats form a microenvironment below which the AOM consortium can operate above the sediment-water interface and carbonate chimneys can, thus, form within an oxic water column. Such microenvironments might permit spatial decoupling of the protons from Reaction 1.8 and the alkalinity produced by AOM (Reaction 1.4), as proposed by Bailey et al. (2009). Peckmann et al. (2004) also documented seep carbonates associated with *Beggiatoa* in a Miocene seep limestone in Italy and concluded that rapid changes from oxic to anoxic conditions facilitated precipitation.

Alternatively, sulfide-oxidizing bacteria can use nitrite (Ettwig et al. 2010) or nitrate as an oxidant (Sayama 2001; Jørgensen and Nelson 2004; Preisler et al. 2007; Himmler et al. 2018):

$$HS^- + NO_3^- + H^+ + H_2O \rightarrow SO_4^{2-} + NH_4^+ \quad (1.9)$$

Reaction 1.9 has been linked to the sulfide-oxidizing bacterium *Thioploca*, and, because it increases the pH, its coupling with the increase in alkalinity produced by AOM (Reaction 1.4) can lead to precipitation of carbonate with a microbial stromatolitic fabric (Himmler et al. 2018).

1.6 Isotope Geochemistry of Cold Seeps

1.6.1 Carbon and Oxygen Isotopes in Seep Carbonates

The delta (δ)-notation for expressing carbon and oxygen isotope ratios involves measurement of the abundance ratios $^{13}C/^{12}C$ or $^{18}O/^{16}O$ in a sample (R_{sample}) and referring them to those of a standard ($R_{standard}$), with values expressed as permil (‰):

$$\delta = \left(R_{sample} / R_{standard} - 1\right) \times 1000 \quad (1.10)$$

The standard used for carbonate O and C isotope notation is historically "Pee Dee Belemnite" or PDB, a fossil cephalopod from the Pee Dee Formation in South Carolina. Once this standard was used up, the measurements were calibrated against standards referable to its laboratory equivalent, Vienna Pee Dee Belemnite (VPDB). Temperature applications express the $\delta^{18}O$ of the water in terms of the seawater standard, Standard Mean Ocean Water or SMOW.

As noted earlier in this chapter, the production of methane by methanogens (Reaction 1.2a) is accompanied by a large C isotope fractionation relative to the carbon isotope composition of the original organic matter (Campbell 2006). The methane so produced is enriched in ^{12}C ($\delta^{13}C = -50$ to -110‰), and the residual CO_2 is enriched in ^{13}C ($\delta^{13}C = +5$ to $+24$‰). Thermogenic methane is enriched in ^{12}C as well but to a lesser extent ($\delta^{13}C = -20$ to -50‰). AOM transfers carbon from methane to the DIC reservoir, imprinting it with low $\delta^{13}C$ values. Carbonates at modern seeps that precipitate from AOM-derived DIC typically have low $\delta^{13}C$ values, and low $\delta^{13}C$ values in presumed fossil seep carbonates are taken as prima facie evidence that the sites indeed represent fossil cold seeps. Additional evidence comes from the molecular fossil inventory in seep-associated carbonates that attest to the presence of lipid biomarkers diagnostic for archaea and bacteria involved in AOM, whose compound-specific carbon isotopes show $\delta^{13}C$ values as low as -120‰ (Peckmann et al. 1999, 2002; Greinert et al. 2002; Elvert et al. 2005: Birgel et al. 2006; Hagemann et al. 2012; Little et al. 2015; Miyajima et al. 2018). A detailed

review of biomarkers at ancient hydrocarbon seeps is beyond the scope of this overview, but the reader is referred to the review by Miyajima and Jenkins (this volume).

During the precipitation of seep carbonates close to the sediment-water interface, other sources of C can contribute to the DIC reservoir and be reflected in the $\delta^{13}C$ values of authigenic carbonates. These additional sources include seawater DIC (−2 to +2‰), C from decomposition of sedimentary organic matter (~−20‰), and a residual CO_2 pool from methanogenesis (+5 to +24‰). The admixture of these sources can produce seep carbonates with a wide range of $\delta^{13}C$ signatures (Natalicchio et al. 2012). For example, Campbell et al. (2002) tabulated $\delta^{13}C$ values ranging from −61‰ to +9‰ in authigenic carbonates from 14 modern seeps. $\delta^{13}C$ values significantly greater than that of ambient DIC likely indicate the incorporation of C from residual CO_2 produced by methanogenesis (Naehr et al. 2007; Roberts et al. 2010). Peckmann and Thiel (2004) suggested that this might occur later in the diagenetic sequence of seep carbonate formation.

The isotope composition of oxygen in seep carbonates also can provide information on the origin of the carbonates. A principal control on $\delta^{18}O$ is the temperature of formation via the well-established temperature-dependent isotope equilibria between O in the water and the precipitated carbonates (Anderson and Arthur 1983; Grossman and Ku 1986; Hudson and Anderson 1989; Stakes et al. 1999), where

$$T(°C) = 16.0 - 4.14\left(\delta^{18}O_c - \delta^{18}O_w\right) + 0.13\left(\delta^{18}O_c - \delta^{18}O_w\right)^2 \quad (1.11)$$

is the temperature equation used for calcite (c) (Anderson and Arthur 1983) and

$$T(°C) = 19.7 - 4.34\left(\delta^{18}O_a - \delta^{18}O_w\right) \quad (1.12)$$

is that for aragonite (a) (Grossman and Ku 1986, as modified by Hudson and Anderson 1989 to express $\delta^{18}O_w$ in terms of SMOW).

The values of $\delta^{18}O_{c,a}$ in Eqs. 1.11 and 1.12 are expressed relative to the VPDB standard (see Eq. 1.10), while that of the water ($\delta^{18}O_w$) is relative to Standard Mean Ocean Water (SMOW). Thus, both mineralogy and fluid composition are factors in these isotope temperature equations. In the case of methane seeps, deep formation waters, including clay dewatering, and water released from the destabilization of methane hydrates can be enriched in ^{18}O and can imprint carbonates with higher $\delta^{18}O$ values than might be predicted from equilibrium precipitation at the ambient temperature of bottom seawater (e.g., Naehr et al. 2007).

An example of the variation in $\delta^{13}C$ and $\delta^{18}O$ observed in ancient seeps is shown in the cross-plot in Fig. 1.5. These data are from authigenic carbonates from seep deposits in the Upper Cretaceous (Campanian) Pierre Shale of North America, which formed in the Western Interior Seaway (WIS) (see Landman et al. this volume, for a list of site localities and more detail on these seeps deposits; data are given in Appendix Table 1.1. These data reveal a broad range in $\delta^{13}C$ values from −5 to −48‰ and a more restricted range in $\delta^{18}O$ values (−0.2 to −1.2‰). The mineralogy is dominated by high-Mg calcite and occasional sparry calcite veins that are the

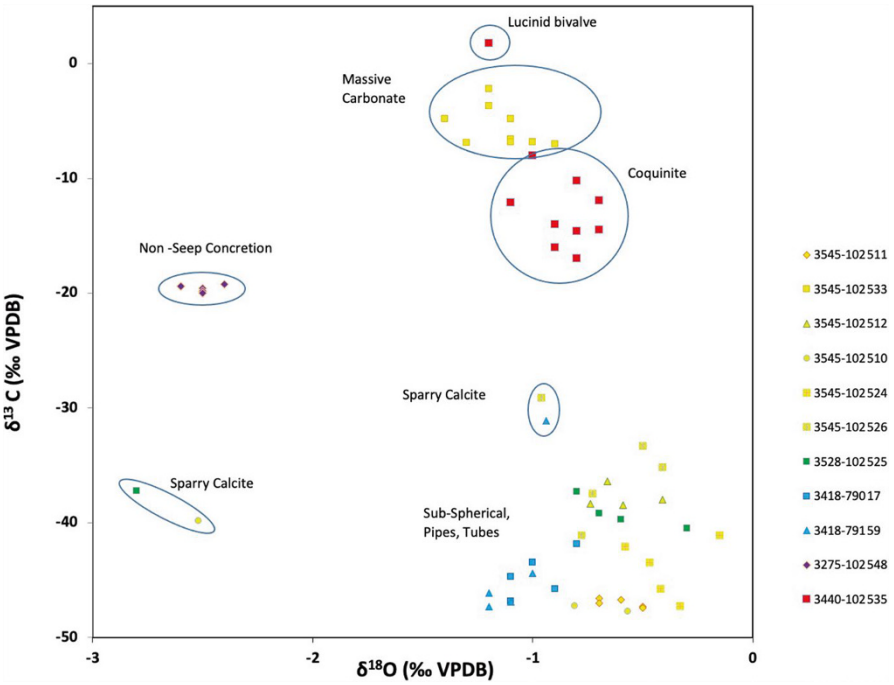

Fig. 1.5 Cross-plot of $\delta^{13}C$ and $\delta^{18}O$ in well-preserved authigenic carbonates from seep deposits collected in the Upper Cretaceous (Campanian) Pierre Shale, South Dakota, USA (Appendix Table 1.1). Seep concretions show a range of $\delta^{13}C$ from ~−48‰ to ~−2‰ (VPDB), reflecting mixtures of different sources of DIC to the precipitated carbonate. Sparry calcite veins in the carbonates are products of later-stage diagenesis. Also plotted are values from a non-seep concretion (AMNH loc. 3275) and lucinid bivalve (AMNH loc. 3440). See text for discussion and Landman et al. (this volume) for information on AMNH localities. Symbols are numbered according to the four-digit AMNH locality, followed by the specimen number. AMNH loc. 3418 is in the *Didymoceras cheyennense* Zone ~74.7 Ma; locs. 3275, 3528, and 3545 are in the *Baculites compressus-B. cuneatus* Zone (~73.5 Ma); and loc. 3440 is in the *Baculites scotti-Didymoceras nebrascense* Zone (~75.6–75.2 Ma)

product of later diagenesis (Handle 2014; Landman et al. 2012; Cochran et al. 2015). Many of the data in Fig. 1.5 were obtained by sequential sampling of seep concretions from the outer surface inward (see Appendix Table 1.1. Variations can be explained by a paragenetic sequence of precipitation as noted by Zwicker et al. (2015; see below). Also shown in Fig. 1.5 are values of $\delta^{13}C$ and $\delta^{18}O$ from a concretion from an age-equivalent non-seep site in the Pierre Shale. These values are distinctly different from those of the seep carbonates and suggest different mechanisms of formation, with precipitation in non-seep concretions associated with organic matter decomposition (e.g., Berner 1968). Concretions with the lowest $\delta^{13}C$ values in Fig. 1.5 are from small, sub-spherical concretions and pipes. Pipes likely formed as AOM proceeded and carbonates precipitated around burrows or methane bubble tubes (Krause et al. 2009; Zwicker et al. 2015), and the high concentration of

methane ensured a strong imprint of methane-derived bicarbonate in the DIC reservoir and precipitated carbonates (Zwicker et al. 2015).

In contrast, massive concretionary bodies and coquinites consisting of cemented layers of *Inoceramus* shells from seep deposits in the Pierre Shale likely formed at or close to the sediment-water interface. As a result, the DIC reservoir from which they formed reflects a mixture of methane-derived DIC and overlying water DIC. Landman et al. (2018) used the $\delta^{13}C$ in well-preserved shells of seep and non-seep ammonites to estimate that the $\delta^{13}C$ of the DIC in the overlying water was +2.7‰ at non-seep sites but was several permil lower, ~ −0.7‰, at seep sites. Additional sources of ^{13}C-enriched DIC include those linked to methanogenesis. The $\delta^{18}O$ values of all the seep carbonates illustrated in Fig. 1.5 suggest precipitation at temperatures typical of bottom water in the WIS, ~20 to 27 °C.

Naehr et al. (2007) observed similar $\delta^{13}C$ and $\delta^{18}O$ patterns in authigenic carbonates found at five continental margin seep sites. They attributed the low $\delta^{13}C$ of many of the high-Mg calcite and aragonite samples to an AOM-derived C source. However, unlike the WIS seep carbonates discussed above, the continental margin seep carbonates studied by Naehr et al. (2007) have $\delta^{18}O$ values that are higher than expected from equilibrium precipitation at bottom-water temperatures and thus suggest an ^{18}O-enriched source, presumably from methane hydrate destabilization. The carbon isotope compositions of dolomites from Monterey Bay and the Santa Barbara and Eel River Basins with higher $\delta^{13}C$ were likely influenced by a ^{13}C-enriched DIC reservoir linked to methanogenesis (Naehr et al. 2007).

Zwicker et al. (2015) demonstrated that a broad range of $\delta^{13}C$ values can occur in a single concretion. Their sampling of pipes from an Oligocene seep deposit (Washington, USA) showed a paragenetic sequence of early-diagenetic carbonate precipitation of matrix micrite and aragonite with very low $\delta^{13}C$ values (<−40‰) that precipitated in the SMTZ as a result of AOM, transitioning to higher $\delta^{13}C$ (>−2.3‰) in later-stage calcite that precipitated in the zone of methanogenesis. Values of $\delta^{18}O$ showed likely equilibrium precipitation with overlying seawater near the sediment-water interface in the early carbonate phases, with more negative values suggesting deeper burial in the later phases.

The rate of methane flux toward the sediment-water interface, position of the SMTZ, pore water-sediment or water-rock interactions, and methane hydrate formation or destabilization can all influence the morphologies and isotopic composition of the precipitated carbonates (Han et al. 2004; Dela Pierre et al. 2010). Methane fluxes can be characterized as effusive (or advective, characterized by high fluid flow) or diffusive (Miyajima et al. 2018). Some of the possible combinations of fluid pathways and sources can be broken down as follows:

- *High methane flux, deep-sourced methane, rapid effusive ascent toward the sediment-water interface (SWI)*: The $\delta^{13}C$ of the DIC of these deep fluids can reflect DIC enriched in ^{13}C from formation of biogenic methane (Reaction 1.2a; $\delta^{13}C$ +8 to +20‰; Han et al. 2004) or with $\delta^{13}C_{DIC}$ closer to 0‰ if from thermogenic methane generation. Such fluids have a high methane concentration (near or at saturation), with a likely $\delta^{13}C_{methane}$ <−50‰. The oxygen isotope composi-

tion of deep fluids can be affected by clay dewatering or reactions with rocks at depth producing ^{18}O-enriched pore fluid, especially for thermogenic sources of methane. Methane hydrate destabilization also would produce ^{18}O-enriched pore fluids. Reactions of the methane-bearing pore water with rock at depth also may alter the Sr or Nd isotope composition of the pore fluid (see Sect. 1.6.4).

The rapid transport of these deep fluids toward and even across the SWI may be facilitated by tectonic activity (such as faulting that opens pathways for deep fluids to flow). Such transport can displace the SMTZ upward, result in the formation of methane bubbles that can escape the sediment through burrows or bubble tubes, and impact the DIC reservoir of the overlying water above the seep. Anaerobic oxidation of methane in the SMTZ results in ^{12}C-enriched DIC that mixes with deep DIC enriched in ^{13}C to produce a higher $\delta^{13}C_{DIC}$ than from AOM alone. Carbonates precipitating near the SWI under these circumstances, thus, may have higher $\delta^{13}C$, and their $\delta^{18}O$ may reflect precipitation at ambient bottom-water temperature and $\delta^{18}O$ composition. Examples of such precipitation are the coquinites and massive carbonates from Late Cretaceous seep deposits of the Pierre Shale (Fig. 1.5). Carbonate precipitation also may occur along fluid escape conduits such as bubble tubes (Krause et al. 2009) or crustacean burrows (Wiese et al. 2015; Zwicker et al. 2015). Methane diffusion away from the main effusive pathway(s) may lead to slower precipitation of smaller sub-spherical concretions with lower $\delta^{13}C$ values resulting from AOM.

- *Deep-sourced methane, slow diffusive flux of methane toward the SWI:* Slow transport of methane in deep-sourced fluids that initially have the characteristics described above provides longer time for the DIC to be influenced by AOM and thus to become more isotopically enriched in ^{12}C. The SMTZ may be displaced to greater sediment depths than in the case of rapid effusive rates of fluid. The $\delta^{18}O$ of the isotopically altered deep pore fluid mixes with that near the sediment-water interface (SWI) pore water and bottom water. Provided that AOM under such conditions is intensive enough to drive local carbonate supersaturation in pore waters, carbonates precipitating under these conditions may have lower $\delta^{13}C$ than those formed from rapid ascent of deep-sourced fluids, as well as $\delta^{18}O$ that more nearly reflects precipitation in equilibrium with near-SWI pore water.
- *Shallow-sourced fluids, rapid effusive transport toward the SWI:* Shallow-sourced fluids likely contain methane dominated by biogenic production, and, therefore, the methane is isotopically highly enriched in ^{12}C ($\delta^{13}C = -50$ to $-110‰$). Rapid ascent can serve to displace the SMTZ toward the SWI, and AOM produces a DIC reservoir that is isotopically enriched in ^{12}C. The $\delta^{18}O$ composition of such fluids reflects that of the shallow sediment pore water. Carbonates precipitated near the SWI under such conditions show perhaps the lowest $\delta^{13}C$ values of the four scenarios described here. The $\delta^{18}O$ of the carbonates reflects precipitation at ambient bottom-water temperatures and oxygen isotope composition.
- *Shallow-sourced fluids, slow diffusive transport of methane toward the SWI:* The methane in these fluids is dominantly biogenic and, thus, strongly enriched in

^{12}C. Because the transport is slow, the SMTZ may be deeper in the sediments. Extensive AOM during diffusion-controlled transport toward the SWI results in a strongly ^{12}C-enriched DIC reservoir. During transport, this can mix with DIC produced from the decomposition of organic matter (e.g., Reaction 1.1) or overlying seawater ($\delta^{13}C_{DIC}$ ~ 0‰), increasing the $\delta^{13}C_{DIC}$. Carbonates precipitated under these conditions may have small sub-spherical morphologies, with low $\delta^{13}C$. Miyajima et al. (2018) described seep deposits from the Neogene of Japan that appear to fit this category. The seeps were characterized by scattered small micritic concretions with $\delta^{13}C$ values ranging from ~ −23 to −46‰. Miyajima et al. (2018) also tabulated other comparable seeps from the Lower Cretaceous to the present day, with $\delta^{13}C$ of micrites ranging from ~ −3 to –50‰.

1.6.2 Carbonate-Clumped Isotopes

As the foregoing illustrates, fluid composition and precipitation temperature are important factors controlling the $\delta^{18}O$ of seep carbonates. The C-O-clumped isotope signature of the carbonates may help resolve these factors for any given seep. Clumped isotope values (Δ_{47}, expressed as ‰) represent the temperature-dependent departure of the abundance of co-occurring ^{13}C and ^{18}O in carbonate relative to that dictated by the statistically predicted abundance of these isotopes in nature. The values of Δ_{47} are independent of fluid composition and, thus, can be used to independently determine the temperature of carbonate precipitation. Together with the carbonate $\delta^{18}O$ signature, this can be used to calculate the $\delta^{18}O$ of the water from which the carbonate precipitated. Loyd et al. (2016) attempted to do this initially for modern seeps for which the temperature and $\delta^{18}O$ of the water were constrained. They found that temperatures determined by the clumped isotope thermometer were up to 50 °C higher than ambient temperatures. Similarly, elevated temperatures were calculated for ancient cold seeps. Loyd et al. (2016) concluded that the clumped isotopes were in disequilibrium relative to the Δ_{47} temperature dependence determined for equilibrium precipitation of calcium carbonate (e.g., Henkes et al. 2013). Possible reasons include mixtures of DIC from distinctly different sources (e.g., DIC from seawater mixed with DIC from AOM), kinetics associated with AOM, or heterogeneous mixtures of carbonate phases in seep carbonates.

More recently, Zhang et al. (2019) measured Δ_{47} values in authigenic carbonates at seeps in the Sea of Japan and Northwest Pacific. They observed that the calculated temperatures were consistent with those of bottom waters at the 300–900-m-deep sites and concluded, in contrast to Loyd et al. (2016), that the carbonates were deposited in clumped isotope equilibrium. Zhang et al. (2019) also calculated $\delta^{18}O$ of the water in which the carbonates precipitated and found that the values were elevated above the ambient bottom water $\delta^{18}O$. They suggested that the oxygen isotope composition of the seep carbonates was influenced by ^{18}O-enriched water released by the destabilization of methane gas hydrates.

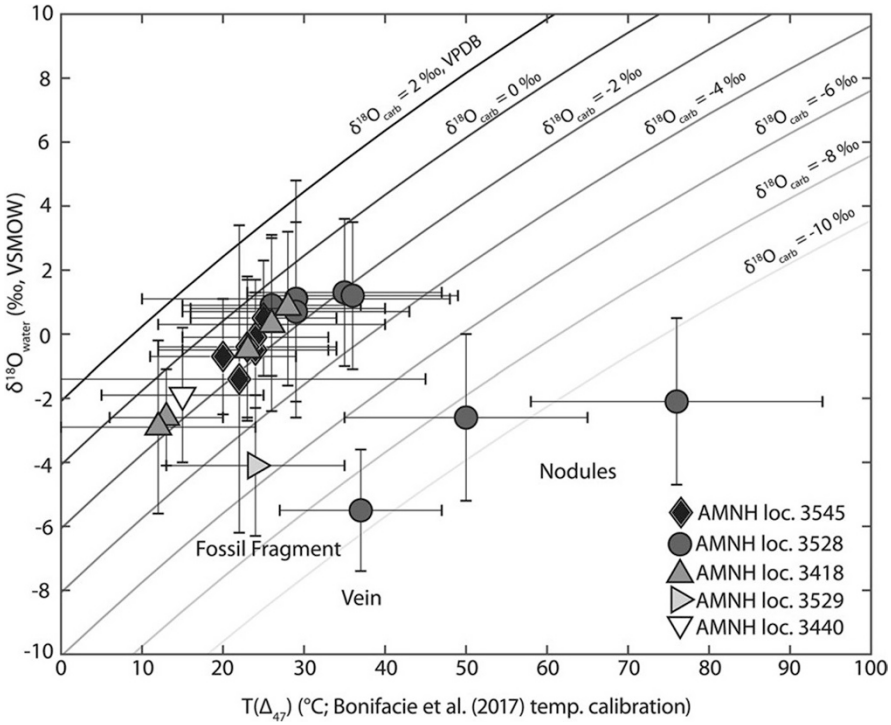

Fig. 1.6 Calculated water oxygen isotope values ($\delta^{18}O_w$) vs. calculated clumped isotope temperatures ($T(\Delta_{47})$) for 21 methane-derived authigenic carbonates from five methane seep deposits in the Upper Cretaceous (Campanian) Pierre Shale, South Dakota, USA. Gray lines represent equilibrium iso-$\delta^{18}O_w$ contours calculated from equilibrium calcite-water oxygen isotope fractionation (Kim and O'Neil 1997). Error bars are calculated based on the propagation of standard deviation of replicate measurements. VSMOW, Vienna standard mean ocean water; VPDB, Vienna Pee Dee Belemnite; AMNH loc., American Museum of Natural History locality (see Landman et al. this volume for details). (Reprinted from Gao et al. 2021 with permission of the Geological Society of America)

Gao (2019) and Gao et al. (2021) documented similar results in seep deposits from the Upper Cretaceous (Campanian) Pierre Shale of North America (Fig. 1.6). Calculated temperatures (23 ± 7 °C) were consistent with other estimates from the Western Interior Seaway, and the authors concluded that the carbonates were precipitated in clumped isotope equilibrium. The calculated $\delta^{18}O$ of the water was −0.5 ± 1.7‰, within error of previous estimates for the WIS and consistent with a time of ice-free conditions on Earth (Shackleton and Kennett 1975). These studies suggest that carbonate-clumped isotopes have a great potential in understanding seep carbonate formation mechanisms, but, clearly, further research is needed.

1.6.3 C and O Isotopes in Shells of Seep Fauna

As described in the preceding section, the carbonates precipitated at cold seeps reflect the different sources of C to the DIC reservoir, from which the carbonate is precipitated. Chief among these is the low $\delta^{13}C_{DIC}$ produced by AOM. Virtually all studies of ancient seeps use the $\delta^{13}C$ of the carbonates to validate that the site was in fact a seep environment. Additional information on the seep environment may be gained through isotope analyses of the shells of mollusks and other carbonate-secreting fauna found at seeps (Lietard and Pierre 2009; Landman et al. 2012, 2018; Cochran et al. 2015). For modern seeps, this is straightforward in that the shells are well-preserved (Lietard and Pierre 2009). Equilibrium precipitation of molluscan shell material from ambient DIC produces $\delta^{13}C$ in the shell carbonate that is ~1‰ and ~2.7‰ greater than that of the DIC for calcite and aragonite, respectively (at 20 °C; McConnaughey 1989). In addition, McConnaughey and Gillikin (2008) showed that metabolically derived (respired) carbon is incorporated into the shell and can account for up to ~30% of the carbon, depending on the mollusk. Lietard and Pierre (2009) measured the O and C isotope composition of bivalves of the genera *Bathymodiolus*, *Calyptogena*, *Vesicomya*, and *Lucina* from both modern cold seeps and hydrothermal vents and also summarized previous measurements from the literature. All the studied bivalves harbored sulfide-oxidizing or methanotrophic bacteria in their tissues (Lietard and Pierre 2009). The values of $\delta^{13}C$ ranged as low as −14‰, and Lietard and Pierre (2009) concluded that ^{12}C-enriched DIC from AOM was partly responsible for the low $\delta^{13}C$ of the shells. Other factors included the mode of life of the bivalves (e.g., infaunal vs. epifaunal) and the influence of the chemosymbionts in the tissues of the organisms. Similarly, Greinert et al. (2002) measured low $\delta^{13}C$ values (−1.83 to −6.50‰) in the solemyid bivalve *Acharax* collected at 4850 m water depth on the Aleutian margin. They acknowledged the possibility of incorporation of low $\delta^{13}C$ metabolic carbon into the shell but concluded that the shells were incorporating carbon from a DIC reservoir that was a mixture of bottom-water DIC and ~4–13% seep fluid DIC. Paull et al. (2008) studied the mussel *Bathymodiolus* from a methane seep and measured $\delta^{13}C$ in both the tissue and shell. They concluded that the shell $\delta^{13}C$ reflected the ambient DIC (which had low $\delta^{13}C$ as a result of AOM) but that the tissue reflected methane-derived C incorporated by methanotrophic bacteria.

Poor preservation of fossil shell material at ancient methane seeps commonly precludes meaningful O and C isotope measurements. However, Landman et al. (2012, 2018), Cochran et al. (2015), and Rowe et al. (2020) reported results on well-preserved shell material from methane seep deposits in the Upper Cretaceous (Campanian) Pierre Shale of South Dakota, USA (see Landman et al. this volume). Preservation was rigorously assessed using scanning electron microscopy (SEM) according to the Preservation Index scale of Cochran et al. (2010), and only the best-preserved shell material was used. Most of the analyses were on ammonites, which lived in the water column above the seeps, and showed $\delta^{13}C$ values as low as −14‰ (Landman et al. 2012).

Cochran et al. (2015) also performed limited sclerochronological sampling of specimens of the Late Cretaceous (Campanian) ammonite *Baculites compressus* collected at seep sites. The low values of $\delta^{13}C$ of these specimens relative to specimens of the same species collected at coeval non-seep sites suggested that the seep ammonites lived and precipitated their shells at the seeps. Other non-isotopic evidence for this conclusion is presented in Landman et al. (this volume). Landman et al. (2018) performed additional sclerochronological sampling of specimens of *B. compressus* from coeval seep and non-seep sites in the same formation (Fig. 1.7). Their results showed a significant offset between the specimens from seep and non-seep sites. Significantly, the C isotope data for the seep ammonites implied that the low $\delta^{13}C_{DIC}$ produced in the sediments from AOM was imprinted on the overlying water column in which the animals lived. An active food web likely developed at the seeps, and the ammonites were attracted to the abundant food there. Indeed, juvenile specimens of *B. compressus* preserved at the seep sites also showed low $\delta^{13}C$ values (Rowe et al. 2020). Both the DIC and the carbon in the food web were likely enriched in ^{12}C, and either DIC- or metabolically-derived carbon (or both) incorporated into the shells produced the lower $\delta^{13}C$ in the seep ammonites relative to non-seep ammonites. The sclerochronological data (Fig. 1.7) support the hypothesis that these animals spent extended time at the seeps. The isotope data, as well as the large number of ammonites collected at seeps from the relatively shallow WIS (Fig. 15.16 in Landman et al. this volume), demonstrate that ammonites, although not seep-obligate fauna, were nevertheless an important component of the Late Cretaceous WIS seep ecosystems.

1.6.4 Strontium and Neodymium Isotopes

Clues to the origin and transport of methane-bearing fluids at seep sites have been gained from the measurement of strontium and neodymium isotopes in seep carbonates. Seeps that occur in tectonically and magmatically active areas can display patterns of $^{87}Sr/^{86}Sr$ and $^{143}Nd/^{144}Nd$ ratios in the authigenic carbonates that indicate the involvement of deep-sourced fluids (Greinert et al. 2002; Joseph et al. 2012; Jakubowicz et al. 2015a, 2019, 2020, 2021). This is particularly the case for active plate margins, at which igneous materials with distinct Sr and Nd isotope signatures are commonly present in the plumbing systems feeding seeps. For example, Greinert et al. (2002) measured $^{87}Sr/^{86}Sr$ values less than the seawater value in seep carbonates from a deep-water seep on the Aleutian margin. They hypothesized that interactions between deep-sourced fluids and oceanic crust produced fluids with low $^{87}Sr/^{86}Sr$ as well as low $\delta^{18}O$, as ^{18}O was preferentially incorporated into altered volcanic glass. Similarly, Hein et al. (2007) observed low $^{87}Sr/^{86}Sr$ in barites and host rocks (dolomites) from the Southern California Borderland. The fluids were likely hydrothermal in origin and exchanged Sr with a less radiogenic strontium source. The low ratios were evident in authigenic carbonates even in cold seep portions of the system. Carbonates with $^{87}Sr/^{86}Sr$ lower than ambient seawater were

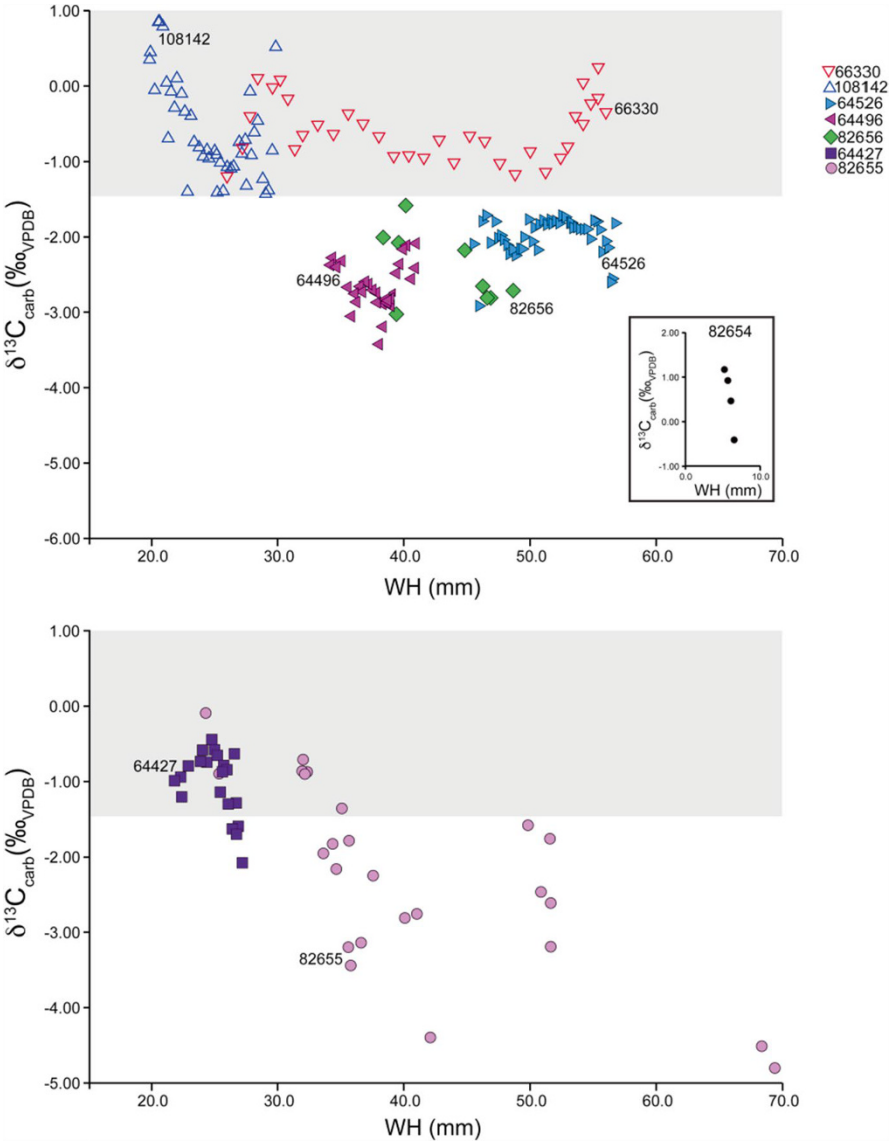

Fig. 1.7 $\delta^{13}C$ (‰ VPDB) from sclerochronological sampling of specimens of *Baculites compressus* from seep deposits (AMNH locs. 3545 and 3528) and coeval non-seep deposits (AMNH locs. 3383 and 3415) in the Upper Cretaceous (Campanian) Pierre Shale, plotted against whorl height (WH). Upper panel: Solid symbols = seep specimens; open symbols = non-seep specimens. Gray area demarcates the isotope values characteristic of the non-seep environment. Lower panel: Seep specimens in which the values of $\delta^{13}C$ in early ontogeny suggest that the animals lived in a non-seep environment (gray area) but migrated into a seep environment as ontogeny progressed (as indicated by increasing whorl height). (Reprinted from Landman et al. 2018 with permission of the American Journal of Science)

found in authigenic carbonates from the Cascadia convergent margin by Joseph et al. (2012), who hypothesized that these involved deep-sourced fluids had exchanged with oceanic-type crust making up the Siletzia terrane, which comprises the basement for much of the Cascadia forearc. The presence of exotic, ^{87}Sr-depleted fluids that interacted with Siletzia apparently characterized the Cascadia subduction zone from an early stage of its activity, as implied by Sr isotope analyses of mid-Eocene (Jakubowicz et al. 2019) and Oligocene (Joseph et al. 2012) seep carbonates of this area. In other instances, the ^{87}Sr/^{86}Sr of seep carbonates provides evidence for shallow, near-SWI precipitation. For example, Joseph et al. (2012) also found ^{87}Sr/^{86}Sr comparable to coeval seawater in Cascadia margin carbonates, indicating multiple sources and flow paths of fluids in that system. A similar, shallow precipitation of seep carbonates was hypothesized by Peckmann et al. (2001) for seeps in the northwestern Black Sea, in which the ^{87}Sr/^{86}Sr of the carbonates was comparable to the ^{87}Sr/^{86}Sr of ambient seawater.

In Upper Cretaceous seep deposits in North America, well-preserved authigenic carbonates also display ^{87}Sr/^{86}Sr different from coeval seawater, but in contrast to the studies cited above, the values are elevated. Figure 1.8 shows ^{87}Sr/^{86}Sr values relative to the coeval seawater value for the WIS (McArthur et al. 1994), expressed as

$$\varepsilon_{Sr} = \left[\left(\frac{87Sr}{86Sr} \right)_{\text{sample}} - \left(\frac{87Sr}{86Sr} \right)_{\text{seawater}} \right] \times 10^6 \tag{1.13}$$

Cochran et al. (2015) hypothesized that the source of the elevated ^{87}Sr/^{86}Sr was due to equilibration/exchange of seep fluids at depth with granitic rocks that now comprise the Black Hills. For example, the Harney Peak granite has ^{87}Sr/^{86}Sr ratios of 0.833520 ± 50 to 2.104340 ± 130 (Walker et al. 1986) or, expressed as ε_{Sr} values, 1.259×10^5 to 1.3067×10^6. In contrast, the Pierre Shale sediments through which the seep fluids transited have low ^{87}Sr/^{86}Sr values, generally <0.7075 (or $\varepsilon_{Sr} = -200$; Cochran et al. 2003). As the seep fluids ascended through the deposit, they mixed with pore water and, near the sediment-water interface, with seawater ($\varepsilon_{Sr} = 0$). Without knowledge of end-member Sr concentrations, it is not possible to discern the relative proportions of the different source contributions at these sites. However, ε_{Sr} values as high as +800 in the seep carbonates (Fig. 1.8; Appendix Table 1.1) indicate the involvement of deep fluids in the seep system. Lower ^{87}Sr/^{86}Sr ratios are evident in sparry calcite filling veins in the carbonates (Fig. 1.8), suggesting that the calcitic veins precipitated later in diagenesis. Lesser, but still significant, elevations in ^{87}Sr/^{86}Sr ratios (ε_{Sr} = ~+50 to +100) were observed in the shells of some ammonites and bivalves collected at the same sites (Cochran et al. 2015). These data, taken together, suggest that deep-sourced fluids were transported through the muddy sediments of the WIS, likely controlled by tectonic activity. Overall, the potential presence of fluid end-members with Sr isotope compositions deviating notably from that of coeval seawater places important constraints on using this isotope system as a stratigraphic tool (cf. Naehr et al. 2007; Kiel et al. 2014; Argentino et al. 2019). Given that many fossil seep deposits formed along former active plate margins, the

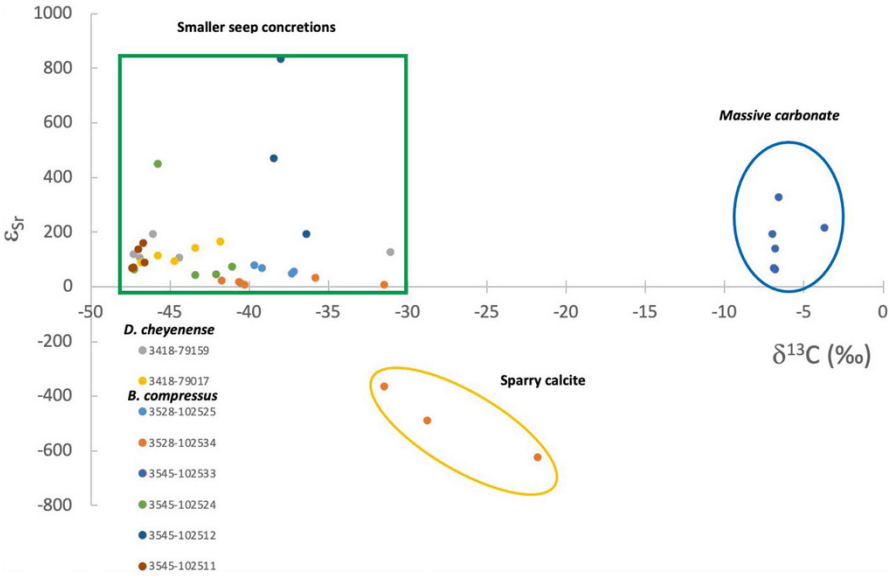

Fig. 1.8 Cross-plot of $^{87}Sr/^{86}Sr$ and $\delta^{13}C$ (‰ VPDB) in well-preserved seep carbonates from the Upper Cretaceous (Campanian) Pierre Shale, South Dakota (Appendix Table 1.1). Sr isotope ratios are plotted as ε_{Sr} (ppm) relative to coeval seawater $^{87}Sr/^{86}Sr$ (see Eq. 1.13). Values of ε_{Sr} >0 ppm suggest that deep fluids interacted with ^{87}Sr-rich granitic rock at depth and were involved in carbonate formation near the sediment-water interface. Sparry calcite veins in the concretions represent later-stage diagenesis. Uncertainty in the ε_{Sr} values is ~±15–20 ppm. Numbers refer to AMNH locality and specimen numbers. See Fig. 1.4 and Appendix Table 1.1 for $\delta^{18}O$ data and the age of the *Didymoceras cheyennense* (AMNH loc. 3418) and *Baculites compressus* (AMNH locs. 3545 and 3528) Zones

likelihood of such deep-seated, exotic Sr involvement must always be evaluated on a case-by-case basis.

Neodymium isotopes ($^{143}Nd/^{144}Nd$) can provide information on the source and nature of transport of seep fluids in a fashion much like $^{87}Sr/^{86}Sr$. Neodymium is a rare earth element, and ^{143}Nd, like ^{87}Sr, is a radiogenic isotope, derived from radioactive decay of ^{147}Sm. The $^{143}Nd/^{144}Nd$ ratio is commonly expressed relative to a standard (CHUR, Chondritic Uniform Reservoir), as ε_{Nd}:

$$\varepsilon_{Nd} = \frac{\left(\frac{143Nd}{144Nd}\right)_{sample} - \left(\frac{143Nd}{144Nd}\right)_{CHUR}}{\left(\frac{143Nd}{144Nd}\right)_{CHUR}} \times 10^4 \tag{1.14}$$

Continental and oceanic crustal rocks have different ε_{Nd} signatures, with low values in continental crust and higher values in oceanic basalts. In the modern ocean, ε_{Nd} varies from ocean basin to ocean basin as a consequence of weathering of different types of source rocks, ranging from −26.6 to +2.7 (Tachikawa et al.

2017). For most basins, ε_{Nd} values are, however, low, globally averaging −8.8 (Lacan et al. 2012). As a tracer of fluid flow at seeps, ε_{Nd} can thus be applied much like ε_{Sr}, with the proviso that, unlike for Sr, establishment of the background seawater ε_{Nd} signature must be made separately for each sedimentary basin, either by direct measurements on water (Bayon et al. 2011; Freslon et al. 2014) or based on mineral proxies (Jakubowicz et al. 2015a, 2019). Considering the dominant sources of rare earth elements, including Nd, to marine pore fluids (see Sect. 1.7.1), for most settings, the pore water ε_{Nd} values can be expected to resemble either the signal from the overlying bottom water (Bayon et al. 2011; Freslon et al. 2014), reflecting dissolution of authigenic, seawater-derived minerals and remineralization of organic matter, or can be expected to be shifted toward higher values, indicative of alteration of silicates (Ge et al. 2020). Therefore, the greatest utility of the Nd isotope system is at seeps overlying mafic volcanic rocks that have an ε_{Nd} signature distinctly different from that of coeval seawater.

Jakubowicz et al. (2015a) made the first such application of Nd isotopes to fossil seeps. They measured rare earth elements (REEs) and $^{143}Nd/^{144}Nd$ ratios in Devonian-age seep carbonates from the Anti-Atlas Mountains of Morocco. They observed that microspar carbonates have higher radiogenic $^{143}Nd/^{144}Nd$ signatures (higher ε_{Nd}) than the coeval seawater value reconstructed from conodonts. They postulated that interactions between ascending seep fluids and a Lower Devonian volcaniclastic unit enriched the fluid in ^{143}Nd. Similar to the observations concerning the Sr isotopes in the sparry calcite veins in the Upper Cretaceous seep carbonates cited above, Jakubowicz et al. (2015a) found less radiogenic Nd isotope signatures in sparry calcite crystals in the Devonian seep carbonates and suggested that these formed under conditions of reduced fluid seepage.

More recently, Jakubowicz et al. (2019) measured ε_{Nd} (as well as $^{87}Sr/^{86}Sr$ and $\delta^{13}C$) in micritic carbonates from a Lower Cretaceous (Barremian) seep deposit that was underlain shallowly by mafic volcanic rocks. The results clearly showed that the carbonates were influenced by mafic signatures of ε_{Nd} and $^{87}Sr/^{86}Sr$, relative to coeval seawater values (Fig. 1.9). Seep fluids that interacted with the rocks displayed an imprint of elevated ε_{Nd} and lower $^{87}Sr/^{86}Sr$ than coeval seawater. Jakubowicz et al. (2021) also showed departures of ε_{Nd} from seawater values in middle Cretaceous seep deposits from the Basque-Cantabrian Basin. The seeps were underlain by igneous intrusions, and Jakubowicz et al. (2021) used the patterns of ε_{Nd} and $\delta^{13}C$ to discern the variety of spatial and temporal differences in fluid flow and composition, as described in Sect. 1.6.1. Thus, both Nd and Sr isotopes help inform the nature of fluid systems at seeps and provide important information not easily obtained from C or O isotope analyses.

1.6.5 Sulfur Isotopes

Fractionation among sulfur isotopes offers clues to sulfur cycling and iron sulfide formation at seeps. The δ-notation used for sulfur is similar to that for C and O:

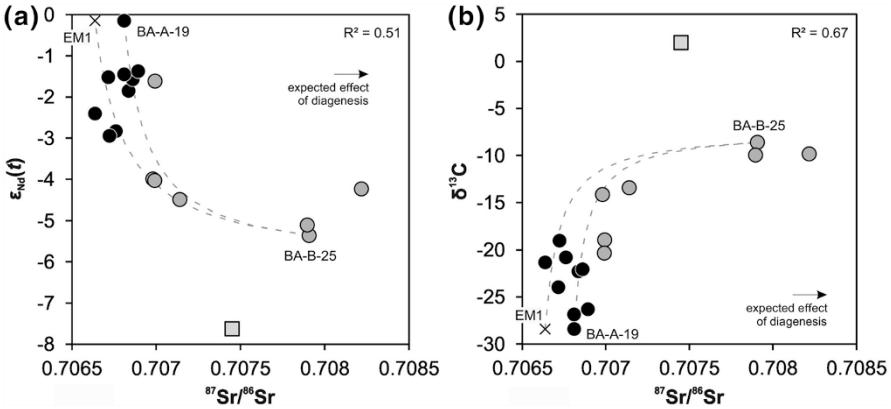

Fig. 1.9 Cross-plots of (**a**) $^{143}Nd/^{144}Nd$ (as ε_{Nd}; Eq. 1.14) vs. $^{87}Sr/^{86}Sr$ and (**b**) $\delta^{13}C$ vs. $^{87}Sr/^{86}Sr$ in Early Cretaceous (Barremian) seep carbonates from the Czech Republic. Also plotted are values corresponding to the isotope composition of contemporaneous local seawater. Coeval seawater values are indicated by the solid gray square. Dashed lines are calculated mixing curves with a mafic rock end-member that has high ε_{Nd} and low $^{87}Sr/^{86}Sr$. Two hypothetical simple mixing scenarios between seep and diagenetic carbonates are shown. The assumed end-members are samples BA-A-19 and BA-A-25, and a hypothetical seep carbonate end-member having the highest ε_{Nd} and lowest $^{87}Sr/^{86}Sr$, $\delta^{13}C$, and $\delta^{18}O$ values observed among the samples. Arrows show trends in which the primary signals shift for diagenetic alteration involving isotopic exchange during fluid-rock interaction, rather than mixing between different cement generations. (Reprinted from Jakubowicz et al. 2019 with permission of Elsevier)

$$\delta^{34}S = \left(R_{sample} / R_{standard} - 1\right) \times 1000 \tag{1.15}$$

where R_{sample} is the $^{34}S/^{32}S$ ratio measured in the sample and $R_{standard}$ is the $^{34}S/^{32}S$ of the standard (Canyon Diablo Troilite; CDT). Organoclastic sulfate reduction produces elevated $\delta^{34}S$ in the residual sulfate reservoir. The sulfide produced has a lower $\delta^{34}S$, and precipitation of iron sulfides generally reflects the $\delta^{34}S$ of the dissolved sulfide. Factors influencing the fractionation include availability of an organic substrate and the sulfate concentration. Maximum fractionations between the sulfate and sulfide reservoirs produced by organoclastic sulfate reduction are ~45‰ (Kaplan and Rittenberg 1964). Higher values likely reflect sulfide oxidation and bacterially mediated disproportionation of reduced sulfur intermediates. Thus, $\delta^{34}S$ values in pyrite ranging down to −45‰ and lower suggest sulfide production from organoclastic sulfate reduction and subsequent reactions (Peckmann et al. 2001; Peckmann and Thiel 2004: Jenkins et al. 2007). In contrast, higher $\delta^{34}S$ in seep pyrite values reflects a ^{34}S-enriched dissolved sulfide reservoir such as might occur in low concentrations of sulfate in the SMTZ (Lin et al. 2016). Indeed, detailed sampling of pyrite from seeps in the South China Sea by SIMS reveals a range of $\delta^{34}S$ value that suggests both organoclastic sulfate reduction and sulfate reduction via AOM are affecting the values during different stages of diagenesis (Lin et al. 2017a, b).

1.7 Elemental Geochemistry of Cold Seeps

1.7.1 Rare Earth Elements

Aside from studies utilizing isotopes of Nd in seeps, a number of new insights have been gained recently by analyzing concentration patterns of rare earth elements [REEs = lanthanides, i.e., elements with atomic numbers 57–71: light REE (LREE) – La, Ce, Pr, Nd; middle REE (MREE) – Sm, Eu, Gd, Tb; heavy REE (HREE) – Dy, Ho, Er, Tm, Yb, Lu]. In terms of their chemical parameters, REEs form a coherent set of elements with similar electronegativities, effective ionic radii decreasing systematically from La to Lu, and, with the exception of Ce and Eu, exist in the trivalent oxidation state (Elderfield 1988; Byrne and Sholkovitz 1996). Changes in REE concentrations across the lanthanide series, as well as variations in the contents of individual REEs, most notably the redox-sensitive Ce and Eu, therefore offer clues to the environmental conditions at which seep carbonates form, including the redox-driven biogeochemical reactions (with implications for the precipitation depth and flow regime; Feng et al. 2009a, b; Ge et al. 2010; Birgel et al. 2011; Wang et al. 2014), and the potential presence of fluid end-members enriched in volcanic-derived components (Jakubowicz et al. 2015a). To facilitate comparison of general trends, REE contents are typically normalized to concentrations found in an average shale (most commonly, Post-Archean Australian Shale – PAAS; McLennan 1989).

Seep carbonates show a broad variability of both total REE concentrations ($\sum$REE) and shale-normalized REE patterns. The highest $\sum$REE are usually shown by microcrystalline cements (micrite/microspar), with an order-of-magnitude lower value typifying sparry crystals (e.g., Himmler et al. 2010; Birgel et al. 2011; Jakubowicz et al. 2015a). Both these features can be attributed to differences in, on the one hand, the environment of carbonate precipitation and, on the other, textural influences on REE acquisition. Being precipitated within pore spaces of background deep-water, typically argillaceous sediments, the microcrystalline carbonates are subjected to high, early-diagenetic influx of REE from reduction of Fe-Mn oxyhydroxide coatings on mineral grains and from remineralization of sedimentary organic matter (Himmler et al. 2010, 2013; Rongemaille et al. 2011; Bayon et al. 2011). A large part of REE uptake by calcite takes place via adsorption onto the crystals, rather than direct substitution for Ca^{2+} in the crystal lattice (Stipp et al. 2003; Lakshtanov and Stipp 2004; Hellebrandt et al. 2016), and thus incorporation of increased REE contents is favored by the high surface-area-to-volume ratio typical of micritic crystals. Indeed, the trend toward increasing REE concentrations with decreasing crystal size is typical also for non-seep carbonates (e.g., Pichler and Veizer 2004; Nothdurft et al. 2004; Webb et al. 2009). Finally, adsorption of larger quantities of REE is facilitated by the kinetic effect associated with the relatively slow precipitation rates typical of micritic carbonates (Ge et al. 2010). Among the sparry carbonate phases, early fibrous cements are most characteristic of areas with focused fluid flow, commonly occluding open spaces present within the micritic

matrix. This, in combination with their rapid growth rate, results in incorporation of lower REE contents (e.g., Feng et al. 2009a; Birgel et al. 2011; Crémière et al. 2016). The lowest ∑REE are typically observed in blocky spar crystals that infill central parts of cavities found in many ancient seep deposits (e.g., Feng et al. 2009b; Jakubowicz et al. 2015a), reflecting the decreasing REE contents of pore fluids with increasing burial, together with progressive REE uptake by precipitating authigenic minerals (cf. Soyol-Erdene and Huh, 2013).

Unlike the case of open-marine and biogenic carbonates precipitated from oxic seawater and usually typified by low ∑REE, the generally high primary REE contents of early-diagenetic seep carbonates make them much less susceptible to significant alteration of their original signatures under marine-burial diagenesis (see discussion in Jakubowicz et al. 2015b). As a result, the REE patterns observed in modern and fossil seep carbonates share notable similarities (Feng et al. 2009b; Jakubowicz et al. 2015a; Wang et al. 2018). Nevertheless, the complex sedimentary environment of seep deposits, including the possible multistage modes of their formation, may make disentangling the signatures imposed by different biogeochemical redox processes difficult (Zwicker et al. 2018; Smrzka et al. 2020).

The shale-normalized REE patterns of seep precipitates are typically distinct from those of oxygenated seawater, characterized by significant HREE-enrichment and strong negative Ce anomalies (Elderfield 1988). The REE incorporation into seep carbonates is controlled by a succession of anaerobic microbial redox processes, involving gradual decomposition of organic matter by the use of progressively less energetically favorable electron acceptors (see Sect. 1.2) and associated intense element remobilization from both mineral and organic substrates (Smrzka et al. 2020). The most common are flattish-to-MREE-enriched patterns, the latter commonly referred to as the "MREE bulge" (Fig. 1.10). This can be attributed

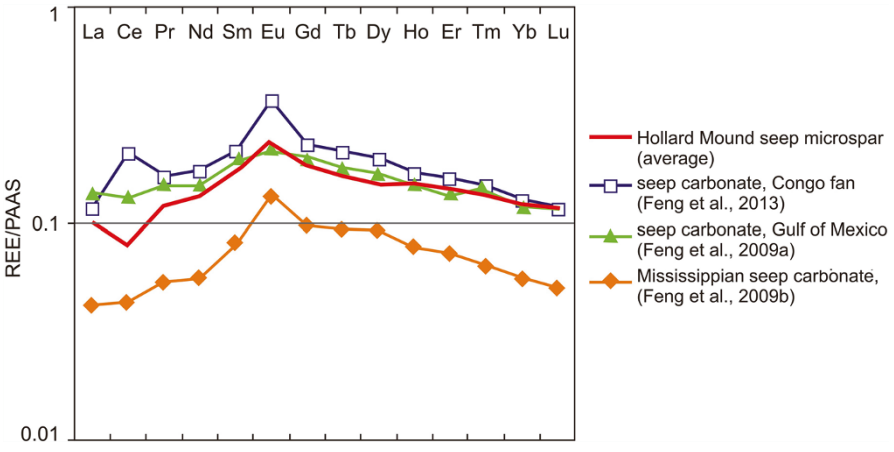

Fig. 1.10 Comparison of the PAAS (post-Archean Australian Shale)-normalized REE patterns in the Holland Mound seep (Middle Devonian, Morocco; average pattern for the microsparitic samples) with selected modern seep carbonates. See text for discussion. (Reprinted from Jakubowicz et al. 2015a, with permission of Elsevier)

mostly to the typical seep carbonate precipitation from anoxic sediment pore waters, rather than open, oxygen-rich seawater. As a result, the main phase of seep carbonate precipitation corresponds to the moment at which large quantities of REEs are released to pore fluids by reduction of Fe-Mn oxides, with their characteristic MREE enrichment (Himmler et al. 2010; Rongemaille et al. 2011; cf. Haley et al. 2004; Kim et al. 2012; Abbott et al. 2016). More rarely, LREE enrichment has been reported, a feature possibly reflecting preferential release of LREE from early-diagenetic decomposition of organic matter (Zwicker et al. 2018, Smrzka et al. 2019; cf. Sholkovitz et al. 1989; Haley et al. 2004; Kim et al. 2012). Finally, HREE enrichment resembling that of seawater has occasionally been observed in some sparry carbonate phases (Zwicker et al. 2018), as well as in pore fluids below the zone of anaerobic oxidation of methane (Kim et al. 2012; Soyol-Erdene and Huh 2013). The origin of the latter pattern, documented relatively recently, remains unclear; possibly, it reflects LREE complexation by increasingly altered organic matter during remineralization of particulate organic carbon and carbonate precipitation from residual, relatively HREE-enriched pore fluids (Himmler et al. 2010; Kim et al. 2012; Zwicker et al. 2018; cf. Haley et al. 2004; Pourret et al. 2008). Other explanations include continuous reduction of Fe oxyhydroxides, complexation by carbonate species, as well as silicate mineral diagenesis (Soyol-Erdene and Huh 2013). For ancient seeps, such HREE-enriched patterns have been observed in texturally and chemically altered carbonates interpreted as a product of early-diagenetic calcification of organic-rich aragonite and may represent a signature imposed on pre-existing carbonates during their early neomorphism, most likely in the zone of methanogenesis (Zwicker et al. 2018).

Because of the small, gradually changing differences in chemical properties among most REEs, they share general similarities in their complexation and surface adsorption behavior in geochemical reactions in modern oceans and sediment pore waters (Elderfield 1988; Byrne and Sholkovitz 1996). Two notable exceptions are Ce and Eu, which can undergo active redox cycling associated with changes in their valence state under near-surface conditions, resulting in their decoupling from the other invariably trivalent REEs. Because under oxic conditions, Ce is rapidly oxidized to reactive Ce^{4+} ions and scavenged by Fe-Mn oxides, a characteristic feature of phases derived from oxygenated seawater is their Ce depletion relative to the neighboring REEs (Byrne and Sholkovitz 1996). Under anoxic conditions, Ce is reduced to soluble Ce^{3+} ions and released into solution, resulting in the Ce enrichment commonly observed in anoxic pore waters (Sholkovitz et al. 1989; German and Elderfield 1990; Tostevin et al. 2016). Indeed, the presence of positive Ce anomalies has been reported for some seep carbonates (Feng et al. 2010; Birgel et al. 2011; Argentino et al. 2019) and pore fluids (Bayon et al. 2011; Himmler et al. 2013), providing insights into spatial and temporal variability of redox conditions in seepage-affected environments. This enrichment is, however, not universal; at many seeps, negative Ce anomalies have been documented in otherwise non-seawater REE patterns, and for some seep deposits, no phases with marked Ce enrichment have been observed (Jakubowicz et al. 2015a and references therein; Fig. 1.10). Factors preventing development of positive Ce anomalies in an environment

apparently favorable for pore water Ce enrichment are the subject of active debate. Among possible explanations are the possible roles of episodic decrease in the flux of methane-rich fluids and associated carbonate precipitation under oxic conditions (Feng et al. 2009b), regular recharge of seawater required for AOM as a source of sulfate (Jakubowicz et al. 2015a), or high alkalinity combined with increased complexation of Ce by organic compounds (Pourret et al. 2008; Himmler et al. 2010; Birgel et al. 2011; Kim et al. 2012).

Cycling of Eu is less understood, and, hence, interpretation of Eu anomalies is commonly problematic. Development of a positive Eu anomaly in a fluid during fluid-rock interactions can proceed through reduction of Eu^{3+} to Eu^{2+}, which is more soluble than trivalent REEs. Such a reduction requires typically high-temperature conditions (>200 °C; Sverjensky 1984), and, therefore, this origin of Eu enrichment is most characteristic of hydrothermal fluids and precipitates (Bau et al. 2010). At relatively low temperatures typifying most hydrocarbon discharges, a more likely source of Eu enrichment is dissolution of Eu-enriched minerals found in mafic igneous rocks, such as plagioclase, provided that such igneous materials are present in the plumbing systems feeding the seeps (Fig. 1.10; Kim et al. 2012; Jakubowicz et al. 2015a). Aside from igneous Eu sources, positive Eu anomalies may develop in authigenic minerals precipitating in non-hydrothermal environments under very strongly reducing, alkaline conditions (Sverjensky 1984; MacRae et al. 1992). For seeps, the latter scenario is facilitated by the high influx of reduced compounds and shallow depth of the sulfate reduction zone, which often results in development of extremely reducing conditions in interstitial waters (Jakubowicz et al. 2015a). Distinguishing these possible sources of Eu enrichment that appear in shale-normalized REE patterns of seep carbonates is additionally hampered by the possibility of developing Eu anomalies as analytical artifacts, because of an interfering effect of BaO on Eu in the course of ICP-MS measurements (Dulski 1994). This possibility should always be considered for seep deposits, which commonly contain an admixture of barite; ideally, REE analyses should be accompanied by measurements of Ba concentrations. Aside from the efforts to constrain mechanisms governing the incorporation of Ce and Eu in seep carbonates, the main focus of recent research in seep-related REE studies includes using REE to better understand the pathways of early-diagenetic processes recorded by different authigenic phases present at seeps (Zwicker et al. 2018), as well as to provide means for identifying fossil seeps discharging a significant amount of longer-chain hydrocarbons (Smrzka et al. 2016, 2019).

1.7.2 Non-lanthanide Elements

In addition to REE, a number of different elemental systems have been measured in seep deposits. Traditionally, minor elements, notably Fe, Mn, Sr, and Mg, have been used as tracers of post-depositional processes and, in particular, to assess the level of diagenetic alteration (with progressive alteration marked by an increase in Fe and Mn and decrease in Sr and Mg concentrations; e.g., Popp et al. 1986; Denison et al. 1994; Brand 2004; Jakubowicz et al. 2015b). However, for methane seeps, application of these elements to constrain diagenetic modifications of primary signatures is

considerably complicated by the complex, mostly anoxic environment of seep carbonate authigenesis. For normal-marine, oxic seawater-derived carbonates, Fe and Mn concentrations are typically very low (<200 ppm for Mn and 600 ppm for Fe; Denison et al. 1994; Brand et al. 2003), because Fe(III) and Mn(IV) must be anaerobically reduced to Fe(II) and Mn(II), respectively, in order to be incorporated into the carbonate crystal lattice. As a result, the enrichment of normal-marine carbonates in Mn and Fe is typically indicative of their post-depositional alteration (Denison et al. 1994; Brand 2004; Boggs and Krinsley 2006). Because seep carbonates precipitate from anoxic interstitial waters in the SMTZ, typically underlying the zones of active microbial Fe(III) and Mn(IV) reduction, the enrichment of seep carbonates in Mn(II) and/or Fe(II) can be a primary feature (e.g., Ritger et al. 1987; Kelly et al. 1995; Buggisch and Krumm 2005; Campbell et al. 2002; Joseph et al. 2013; Tribovillard et al. 2013; Kiel et al. 2014; Zwicker et al. 2018; Argentino et al. 2019). This is especially the case for calcite, which has a rhombohedral crystal structure that is more favorable for incorporation of Mn^{2+} than that of orthorhombic aragonite (Reeder 1983; Tucker and Wright 1990). Mn^{2+} and Fe^{2+} ions also can be directly supplied to the precipitating carbonates due to AOM itself because, in addition to sulfate, Mn(IV) and Fe(III) can also serve as oxidants in this process (see Sect. 1.3; Beal et al. 2009).

One important, yet rarely acknowledged consequence of this is that cathodoluminescence, commonly applied as a cost- and time-effective test of the alteration level of normal-marine limestones, cannot be applied in an analogously simple manner for seep carbonates. The main activator of luminescence in carbonate minerals is Mn(II) (Machel 2000; Boggs and Krinsley 2006), and, consequently, the presence of distinct red-to-yellow luminescence may represent an original characteristic of many seep deposits, especially those dominated by calcite. Accordingly, except for the case of neomorphic alteration, primary mineralogical differences may play a role in the observed differences between cathodoluminescence patterns shown by microcrystalline seep carbonates (most often of original high-Mg calcite and commonly showing red-to-orange luminescence) and isopachous-fibrous cements (commonly primarily aragonitic and more often non-luminescent; e.g., Kiel et al. 2014). For fossil seep deposits that underwent long burial histories, the problem of disentangling the primary and diagenetic controls on the carbonate Mn and Fe contents poses major limitations to more advanced applications of these systems, such as reconstructing past redox zonations, imprints of methanogenesis, or element circulation associated with the formation, oxidation, and dissolution of Fe- and Mn-bearing minerals (see Smrzka et al. 2020 and references therein).

Compared with Fe and Mn, primary mineralogical differences are of even greater importance for the variability of Sr and Mg concentrations observed in unaltered seep carbonates (Bayon et al. 2007; Nöthen and Kasten 2011; Tong et al. 2019). The Sr and Mg contents can also be substantially modified by fluid-rock interactions in the course of diagenetic alteration. Both of the main $CaCO_3$ polymorphs making up seep carbonates, aragonite and high-Mg calcite, are metastable and normally stabilize to low-Mg calcite in the course of diagenesis. This process is accompanied by loss of both Sr and Mg (Tucker and Wright 1990). The scales of these alteration effects are different depending upon the original mineralogies of seep carbonate phases, because the crystal lattice of aragonite is favorable for substitution of Sr^{2+},

but not Mg^{2+} into Ca^{2+} structural sites, whereas the opposite applies to high-Mg calcite (Reeder 1983; Finch and Allison 2007). Among the most common applications of Sr and Mg concentration analyses in fossil seep studies is discrimination between the aragonite and high-Mg calcite precursors of low-Mg calcites that comprise the bulk of most ancient seep deposits. This, in turn, provides constraints on paleoenvironmental conditions, most notably former pore water sulfate concentrations and, by inference, fluid flow rates and precipitation depths (e.g., Greinert et al. 2001; Naehr et al. 2007; Nöthen and Kasten 2011; for a general conceptual background, see Burton 1993). The method relies on the assumption that increased concentrations of Sr in low-Mg calcite are indicative of its originally aragonitic mineralogy, whereas low Sr and elevated Mg contents suggest a high-Mg calcite precursor, consistent with the results of many case studies involving a combination of elemental and petrographic analyses (e.g., Savard et al. 1996; Campbell et al. 2002; Buggisch and Krumm 2005; Kiel et al. 2014).

Interpretation of the Sr and Mg concentration data is further hampered by variable diagenetic pathways experienced by different seep deposits and the disparate alteration responses expected for different $CaCO_3$ polymorphs. For example, some post-aragonite calcites that experienced extensive alteration may display Sr contents even lower than those of unaltered low-Mg calcites, whereas diagenetic calcites precipitated from fluids derived from aragonite calcification may show increased Sr concentrations (Banner 1995). In addition, during recrystallization of high-Mg calcite, Sr can be released from Sr-rich mineral impurities, such as aragonite inclusions, which, even if volumetrically small, may have a substantial effect on the bulk Sr concentrations of the alteration product (Banner 1995). For aragonite, diagenetic exchange may, on the other hand, even result in some increase in its Mg contents (cf. Zwicker et al. 2018). The difficulties with unequivocally distinguishing between former aragonite and high-Mg calcite, or mixtures of the two, based on either geochemical or petrographic criteria may hamper conclusive interpretation of the Mg/Sr ratios when these are applied as a measure of the degree of diagenetic alteration (e.g., Zwicker et al. 2018). Therefore, the Sr and Mg isotope analyses of ancient seep carbonates must be carried out in combination with petrological observations, which remain the primary method of reconstructing former fabrics and mineralogies at fossil seeps (cf., Campbell et al. 2002; Peckmann et al. 2007; Joseph et al. 2013).

Aside from the minor elements, seep studies have also applied trace elements. Many of these applications have been made in the past decade but are yet to develop their full potential to allow for their broader use in investigations of fossil seeps. Among the trace elements that may potentially provide insights into the paleoenvironment, a particular focus has recently been on those offered by redox-sensitive elements, such as Mo, U, Cd, Sb, and As. Concentrations of these elements have been used to provide constraints on fluid flux and the dynamics of redox conditions (Mo and Mo/U ratios: Cangemi et al. 2010; Peketi et al. 2012; Hu et al. 2014, 2020; Chen et al. 2016; Williscroft et al. 2017; Deng et al. 2020; Cd: Smrzka et al. 2017; Ba: Torres et al. 2002; Nöthen and Kasten 2011; Hu et al. 2020; Y/Mo ratios: Himmler et al. 2010; Jakubowicz et al. 2015a; Wang et al. 2018). Applications include (a) distinguishing between sulfate-driven AOM and organoclastic sulfate reduction (Mo, As, Sb; Smrzka et al. 2020), (b) identifying seeps with significant involvement of heavy hydrocarbons (Mo/U ratios; Smrzka et al. 2016, 2019), (c)

discriminating between different primary carbonate mineralogies (Mo, U, Cd; Feng and Chen 2015), and (d) tracing elemental recycling associated with the formation and dissolution of Fe- and Mn-bearing mineral phases (As, Sb, Mo, U; Bayon et al. 2011; Tribovillard et al. 2013; Hu et al. 2014; Wang et al. 2019).

As well as these applications, a more traditional approach has been to use conservative lithogenic elements, such as Al, Ti, Sc, Zr, Th, and Hf, to identify elemental release from a terrigenous fraction, either upon seep carbonate precipitation or as contamination during laboratory leaching procedures, and also to use them for normalization of other elements to calculate their authigenic fractions, as they are applied in general carbonate sedimentology (e.g., Nothdurft et al. 2004; Algeo and Li 2020; Smrzka et al. 2020). In general, however, because many trace elements undergo active cycling in various zones of redox processes and may be subject to repeated remobilization, and diagenetic alteration associated with organic matter and clay-mineral diagenesis, interpretation of trace element data in ancient carbonates remains challenging (Algeo and Liu 2020 and references therein). This problem is especially pertinent for studies of hydrocarbon seeps, given their complex and dynamic redox conditions, spatial and temporal fluctuations in the fluid flux, and migration pathways and composition of the seeping fluids. Accordingly, further research is required before the redox-sensitive trace elements can be more broadly applied to address specific, case study-based questions (for an overview, see Smrzka et al. 2020; general reappraisals of the use of trace elements as redox proxies have recently been published by Algeo and Liu 2020; Algeo and Li 2020; and Bennett and Canfield 2020).

1.8 Summary

A fundamental geochemical process operating at methane seeps is the anaerobic oxidation of methane (AOM) by which methane is oxidized and sulfate is reduced. Because both reactants are necessary for AOM to proceed, this process takes place in the sulfate-methane transition zone, generally located below the sediment-water interface. Methane produced biogenically or thermogenically has a low $\delta^{13}C$ signature, and this is transferred to the dissolved inorganic carbon (DIC) reservoir during AOM. As a consequence of the increase in alkalinity from AOM, calcium carbonate supersaturation can occur, and various carbonate minerals can precipitate with low $\delta^{13}C$. Indeed, very low $\delta^{13}C$ values of ancient calcium carbonates are taken as prima facie evidence that the carbonates formed in a cold hydrocarbon seep environment.

Other chemical reactions typical of early diagenesis of organic matter in marine sediments occur at seeps. Two reactions, organoclastic reduction of sulfate (ORS) and Fe(III) reduction, in addition to AOM, provide links between the iron and sulfur cycles. Dissolved sulfide produced by AOM or ORS can react with reduced iron (Fe^{2+}) to form iron monosulfides and eventually pyrite, a mineral frequently associated with carbonates at methane seeps.

Numerous isotope systems have been applied to studies of methane seeps. Carbon isotopes ($\delta^{13}C$) in authigenic seep carbonates provide evidence of the source of the methane (biogenic or thermogenic) and the possibility of admixtures of other sources of DIC that contribute to seep carbonate formation (DIC from overlying

water, ORS, etc.). Carbon isotope measurements of lipid biomarkers in the molecular fossil inventory in seep-associated carbonates provide evidence for the archaea and bacteria involved in AOM. Oxygen isotopes ($\delta^{18}O$) provide information on the temperature of seep formation, the possible influence of methane hydrates on seep development, and seep fluid-rock or fluid-sediment interactions. The application of carbonate-clumped isotopes to seep systems is at a very early stage but offers the possibility of resolving both the temperature of seep carbonate formation and aspects of fluid source and composition. Fractionation among sulfur isotopes, as expressed by $\delta^{34}S$ in sulfide phases, helps reveal the relative importance of reduced sulfur from OSR and AOM in sulfide formation. Strontium ($^{87}Sr/^{86}Sr$) and neodymium ($^{143}Nd/^{144}Nd$) isotopes help clarify the involvement of deep-sourced fluids and fluid pathways in transferring methane to the SMTZ.

New insights into seeps also have been gained by analyzing concentration patterns of rare earth elements (REEs) in seep carbonates. Changes in REE concentrations across the lanthanide series as well as variations of individual REE, notably the redox-sensitive Ce and Eu, provide clues to the environmental conditions under which seep carbonates formed, including the redox-driven biogeochemical reactions involved (with implications for the precipitation depth and flow regime) and the potential presence of fluid end-members enriched in volcanic-derived components.

Concentrations of the minor elements Fe, Mn, Sr, and Mg in seep carbonates reflect mineralogical differences, although the possibility of diagenetic alteration during burial must be considered in their interpretation. Concentration of redox-sensitive trace elements (e.g., Mo, U, Cd, Sb, As) has been used to provide constraints on fluid flux and the dynamics of redox conditions to identify seeps with significant involvement of heavy hydrocarbons, to aid in discrimination between different primary carbonate mineralogies, and to trace elemental recycling associated with the formation and dissolution of Fe- and Mn-bearing mineral phases. Future research into fossil seep systems should maximize the information to be gained by incorporating multiple isotopic and elemental approaches.

Acknowledgments This chapter has benefited enormously from the helpful reviews by Marcello Natalicchio (University of Torino, Italy) and Daniel Smrzka (Universität Wien, Austria). The authors are grateful for the assistance from Shannon Brophy, Alison Rowe, and Remy Rovelli in the field and Bushra Hussaini, Kathleen Sarg, and Mariah Slovacek in the laboratory. Stephen Thurston provided graphic support. The strontium isotope measurements reported in Appendix Table 1.1 were made at the Stony Brook University FIRST Laboratory. We thank Katie Wooton, Troy Rasbury, and Tyler Levitsky for their efforts. We have benefited from stimulating discussions with Corinne Myers and James Witts. This work was partially supported by the Norman D. Newell Fund and the Landman Research Fund of the American Museum of Natural History.

Appendix

Appendix Table 1.1 gives oxygen, carbon, and strontium isotope data measured on seep concretions from three ammonite zones in the Late Cretaceous Western Interior Seaway (WIS) of North America. These data are plotted in Figs. 1.5 and 1.8. The location information (AMNH loc.) is given in Landman et al. (this volume).

Appendix Table 1.1 Oxygen, carbon, and strontium isotope data for Western Interior Seaway seep concretions

AMNH loc.	Ammonite zone	AMNH ID	Concretion type	Mineralogy	Sample number	$\delta^{18}O$ (‰ VPDB)	$\delta^{13}C$ (‰ VPDB)	$^{87}Sr/^{86}Sr$	ε_{Sr}
3545	*Baculites compressus*	102511	~3 cm; spherical	Micrite	1	−0.5	−47.3	0.707747	72
	(73.79 ± 0.36 Ma)			Micrite	2	−0.7	−46.6	0.707765	90
				Micrite	3	−0.5	−47.4	0.707744	69
				Micrite	4	−0.7	−47.0	0.707811	136
				Micrite	5	−0.6	−46.7	0.707835	160
3545	*B. compressus*	102533	Massive carbonate	Micrite	1	−1.3	−6.9	0.707744	69
				Micrite	2	−1.1	−6.6	0.708002	327
				Sparry calcite	3	−1.4	−4.8	0.707810	135
				Sparry calcite	4	−1.2	−2.2	0.707717	42
				Micrite	5	−1.2	−3.7	0.707890	215
				Micrite	6	−0.9	−7.0	0.707869	194
				Sparry calcite	7	−1.1	−4.8	0.707774	99
				Micrite	8	−1.0	−6.8	0.707738	63
				Micrite	9	−1.1	−6.8	0.707816	141
3545	*B. compressus*	102512	~3 cm; spherical	Micrite	1	−0.7	−36.4	0.707868	193
				Micrite	2	−0.4	−38.0	0.708508	833
				Micrite	3	−0.7	−38.3	–	–
				Micrite	4	−0.6	−38.5	0.708146	471
3545	*B. compressus*	102510	~1 cm; tubular	Micrite	1	−0.8	−47.3	–	–
				Sparry calcite	2	−2.5	−39.9	–	–
				Micrite	3	−0.6	−47.7	–	–
3545	*B. compressus*	102524	~7 cm; tubular	Micrite	1	−0.5	−43.4	0.707718	43
				Micrite	2	−0.6	−42.1	0.707721	46
				Micrite	3	−0.4	−45.8	0.708124	449

(continued)

Appendix Table 1.1 (continued)

AMNH loc.	Ammonite zone	AMNH ID	Concretion type	Mineralogy	Sample number	$\delta^{18}O$ (‰ VPDB)	$\delta^{13}C$ (‰ VPDB)	$^{87}Sr/^{86}Sr$	ε_{Sr}
				Micrite	4	−0.3	−47.3	0.707739	64
				Vug	5	−0.2	−41.1	0.707749	74
3545	*B. compressus*	102526	~10 cm; elongate	Sparry calcite	1	−3.1	1.9	–	–
				Micrite	2	−1.0	−29.1	–	–
				Micrite	3	−0.5	−33.3	–	–
				Micrite	4	−0.8	−41.1	–	–
				Micrite	5	−0.7	−37.4	–	–
				Micrite	6	−0.4	−35.1	–	–
3528	*B. compressus*	102525	~10 cm; tubular	Micrite	1	−0.8	−37.3	0.707717	47
				Micrite	2	−0.3	−40.5	0.707682	12
				Sparry calcite	3	−2.8	−37.2	0.707725	55
				Micrite	4	−0.7	−39.2	0.707737	67
				Micrite	5	−0.6	−39.7	0.707750	80
3528	*B. compressus*	102534	~7 cm; elongate pipe	Micrite	1	−6.6	−28.8	0.707181	−489.2
				Micrite	2	−2.0	−35.8	0.707703	33.2
				Micrite	3	−2.0	−40.3	0.707677	7.0
				Micrite	4	−1.8	−31.5	0.707677	6.6
				Spar	5	−13.9	−21.8	0.707047	−623.0
				Micrite/spar	6	−13.6	−31.5	0.707306	−364.5
				Micrite	7	−1.8	−40.6	0.707688	18.1
				Micrite	8	−1.4	−41.7	0.707692	22.4
3275	*B. compressus*	102548	~6 cm; non-seep	Micrite	1	−2.4	−19	–	–

AMNH loc.	Ammonite zone	AMNH ID	Concretion type	Mineralogy	Sample number	$\delta^{18}O$ (‰ VPDB)	$\delta^{13}C$ (‰ VPDB)	$^{87}Sr/^{86}Sr$	ε_{Sr}
				Micrite	2	−2.6	−19	–	–
				Micrite	3	−2.6	−19	–	–
				Micrite	4	−2.5	−20	–	–
				Micrite	5	−2.5	−20	–	–
				Micrite	6	−2.5	−20	–	–
				Micrite	7	−2.5	−20	–	–
3418	*Didymoceras cheyennense*	79159	~10 cm; elongate	Micrite	1	−1.2	−46.1	0.707829	113
	(74.67 ± 0.15 Ma)			Micrite	2	−1.1	−46.9	0.707741	93
				Micrite	3	−1.2	−47.3	0.707755	142
				Micrite	4	−0.9	−31.1	0.707761	89
				Micrite	5	−1.0	−44.4	0.707741	166
3418	*D. cheyennense*	79017	~5 cm; sub-spherical	Micrite	1	−0.9	−45.8	0.707748	113
				Micrite	2	−1.1	−44.7	0.707728	93
				Micrite	3	−1.0	−43.4	0.707777	142
				Micrite	4	−1.1	−46.8	0.707724	89
				Micrite	5	−0.8	−41.8	0.707801	166
3440	*Didymoceras nebrascense*	102535	~10 cm; coquinite	Micrite w/shell material	1	−1.1	−12.1	–	–
	(75.19 ± 0.28 Ma)			Micrite w/shell material	2	−0.9	−16.0	–	–
				Micrite w/shell material	3	−0.8	−17.0	–	–
				Micrite w/shell material	4	−0.7	−14.5	–	–

(continued)

Appendix Table 1.1 (continued)

AMNH loc.	Ammonite zone	AMNH ID	Concretion type	Mineralogy	Sample number	$\delta^{18}O$ (‰ VPDB)	$\delta^{13}C$ (‰ VPDB)	$^{87}Sr/^{86}Sr$	ε_{Sr}
				Micrite w/shell material	5	−0.8	−14.6	–	–
				Micrite w/shell material	6	−0.9	−14.0	–	–
				Micrite w/shell material	7	−1.0	−8.0	–	–
				Lucinid bivalve	8	−1.2	1.8	–	–
				Micrite w/shell material	9	−0.8	−10.2	–	–
				Micrite w/shell material	10	−0.7	−11.9	–	–

Methods Details on the analytical methods are given in Cochran et al. (2003, 2015) and Landman et al. (2012, 2018). Concretions were sampled sequentially from the outside inward, on a scale of approximately 3 mm, with Sample Number = 1 corresponding to the surface of the concretion. Oxygen and carbon isotopes are reported as permil $\delta^{18}O$ and $\delta^{13}C$ as relative to the VPDB standard. Values of ε_{Sr} are calculated from

$$\varepsilon_{Sr} = \left[\left(\frac{87Sr}{86Sr} \right)_{\text{sample}} - \left(\frac{87Sr}{86Sr} \right)_{\text{seawater}} \right] \times 10^6 \tag{1.13}$$

where $(^{87}Sr/^{86}Sr)_{seawater}$ represents the coeval seawater dissolved $^{87}Sr/^{86}Sr$ for the WIS reconstructed by McArthur et al. (1994). Photos of examples of the types of concretions analyzed here are given in Landman et al. (this volume) Figs. 15.12 and 15.13.

References

Abbott AN, Haley BA, McManus J (2016) The impact of sedimentary coatings on the diagenetic Nd flux. Earth Planet Sci Lett 449:217–227

Aharon P (1994) Geology and biology of modern ad ancient submarine seeps and vents: an introduction. Geo-Mar Lett 14:69–73

Algeo TJ, Li C (2020) Redox classification and calibration of redox thresholds in sedimentary systems. Geochim Cosmochim Acta 287:8–26

Algeo TJ, Liu J (2020) A re-assessment of elemental proxies for paleoredox analysis. Chem Geol 540(2):119549. https://doi.org/10.1016/j.chemgeo.2020.119549

Anderson TF, Arthur MA (1983) Stable isotopes of oxygen and carbon and their application to sedimentologic and environmental problems. In: Arthur MA, Anderson TF, Kaplan IR et al (eds) Stable isotopes in sedimentary geology. Society of Economic Paleontologists and Mineralogists Short Course, vol no. 10. Society of Economic Paleontologists and Mineralogists, Tulsa, pp 1–151

Angeletti L, Canese S, Franchi F et al (2015) The 'chimney forest' of the deep Montenegrin margin, south-eastern Adriatic Sea. Mar Pet Geol 66:542–554

Argentino C, Lugli F, Cipriani A et al (2019) A deep fluid source of radiogenic Sr and highly dynamic seepage conditions recorded in Miocene seep carbonates of the northern Apennines (Italy). Chem Geol 522:135–147

Bailey JV, Orphan VJ, Joye SB et al (2009) Chemotrophic microbial mats and their potential preservation in the rock record. Astrobiology 9(9):843–859

Berner RA (1968) Calcium carbonate concretions formed by the decomposition of organic matter. Science 159(3811):195–197

Banner JL (1995) Application of the trace element and isotope geochemistry of strontium to studies of carbonate diagenesis. Sedimentology 42:805–824

Bau M, Balan S, Schmidt K, Koschinsky A (2010) Rare earth elements in mussel shells of the Mytilidae family as tracers for hidden and fossil high-temperature hydrothermal systems. Earth Planet Sci Lett 299(3–4):310–316

Bayon G, Pierre C, Etoubleau J et al (2007) Sr/Ca and Mg/Ca ratios in Niger Delta sediments: implications for authigenic carbonate genesis in cold seep environments. Mar Geol 241(1−4):93–109

Bayon G, Birot D, Ruffine L et al (2011) Evidence for intense REE scavenging at cold seeps from the Niger Delta margin. Earth Planet Sci Lett 312(3/4):443–452
Bayon G, Dupré S, Ponzevera E et al (2013) Formation of carbonate chimneys in the Mediterranean Sea linked to deep-water oxygen depletion. Nat Geosci 6:755–760. https://doi.org/10.1038/NGEO1888
Beal EJ, House CH, Orphan VJ (2009) Manganese- and iron-dependent marine methane oxidation. Science 325:184–187
Bennett WW, Canfield DE (2020) Redox-sensitive trace metals as paleoredox proxies: a review and analysis of data from modern sediments. Earth-Sci Rev 204:103175
Berner RA (1980) Early diagenesis—a theoretical approach. Princeton University Press, Princeton
Birgel D, Peckmann J, Klautzsch S et al (2006) Anaerobic and aerobic oxidation of methane at Late Cretaceous seeps in the Western Interior Seaway, USA. Geomicrobiol J 23:565–577
Birgel D, Feng D, Roberts HH et al (2011) Changing redox conditions at cold seeps as revealed by authigenic carbonates from Alaminos Canyon, northern Gulf of Mexico. Chem Geol 285(1−4):82–96
Boetius A, Ravenschlag K, Schubert CJ et al (2000) A marine consortium apparently mediating anaerobic oxidation of methane. Nature 407:623–625
Boggs S, Krinsley D (2006) Application of cathodoluminescence imaging to the study of sedimentary rocks. Cambridge University Press, Cambridge
Bohrmann G, Torres ME (2006) Gas hydrates in marine sediments. In: Schulz HD, Zabel M (eds) Marine geochemistry. Springer, Heidelberg, pp 481–512
Bonifacie M, Calmels D, Eiler JM et al (2017) Calibration of the dolomite clumped isotope thermometer from 25 to 350° C, and implications for a universal calibration for all (Ca, Mg, Fe) CO_3 carbonates. Geochim Cosmochim Acta 200:255–279. https://doi.org/10.1016/j.gca.2016.11.028
Bowles MW, Mogollon JM, Kasten S et al (2014) Global rates of marine sulfate reduction and implications for sub-sea-floor metabolic activities. Science 344:889–891
Brand U (2004) Carbon, oxygen and strontium isotopes in Paleozoic carbonate components: an evaluation of original seawater-chemistry proxies. Chem Geol 204(1/2):23–44
Brand U, Logan A, Hiller N et al (2003) Geochemistry of modern brachiopods: applications and implications for oceanography and paleoceanography. Chem Geol 198:305–334
Bristow TF, Grotzinger JP (2013) Sulfate availability and the geological record of cold-seep deposits. Geology 41:811–814
Buggisch W, Krumm S (2005) Palaeozoic cold seep carbonates from Europe and North Africa—an integrated isotopic and geochemical approach. Facies 51(1−4):566–583
Burdige DJ (2006) Geochemistry of marine sediments. Princeton University Press, Princeton
Burton EA (1993) Controls on marine carbonate cement mineralogy: review and reassessment. Chem Geol 105:163–179
Byrne RH, Sholkovitz ER (1996) Marine chemistry and geochemistry of the lanthanides. In: Gschneidner KA Jr, Eyring L (eds) Handbook on the physics and chemistry of rare earths. Elsevier Science, Amsterdam, pp 497–593
Campbell KA (2006) Hydrocarbon seep and hydrothermal vent paleoenvironments and paleontology: past developments and future research directions. Palaeogeogr Palaeoclimatol Palaeoecol 232:362–407
Campbell KA, Farmer JD, Des Marais D (2002) Ancient hydrocarbon seeps from the Mesozoic convergent margin of California: carbonate geochemistry, fluids and palaeoenvironments. Geofluids 2:63–94
Cangemi M, Di Leonardo R, Bellanca A et al (2010) Geochemistry and mineralogy of sediments and authigenic carbonates from the Malta Plateau, Strait of Sicily (central Mediterranean): relationships with mud/fluid release from a mud volcano system. Chem Geol 276(3/4):294–308
Cavagna S, Clari P, Dela Pierre F et al (2015) Sluggish and steady focussed flows through fine-grained sediments: the methane-derived cylindrical concretions of the Tertiary Piedmont Basin (NW Italy). Mar Pet Geol 66:596–605

Chen F, Hu Y, Feng D et al (2016) Evidence of intense methane seepages from molybdenum enrichments in gas hydrate-bearing sediments of the northern South China Sea. Chem Geol 443:173–181

Cochran JK, Landman NH, Turekian KK et al (2003) Paleoceanography of the Late Cretaceous (Maastrichtian) Western Interior Seaway of North America: evidence from Sr and O isotopes. Palaeogeogr Palaeoclimatol Palaeoecol 191:45–64

Cochran JK, Kallenberg K, Landman NH et al (2010) Effect of diagenesis on the Sr, O, and C isotope composition of Late Cretaceous mollusks from the Western Interior Seaway of North America. Am J Sci 310:69–88

Cochran JK, Landman NH, Larson NL et al (2015) Geochemical evidence (C and Sr isotopes) for methane seeps as ammonite habitats in the Late Cretaceous (Campanian) Western Interior Seaway. Swiss J Palaeontol 134:153–165

Crémière A, Lepland A, Chand S et al (2016) Fluid source and methane-related diagenetic processes recorded in cold seep carbonates from the Alvheim channel, central North Sea. Chem Geol 432:16–33

Dela Pierre F, Martire L, Natalicchio M et al (2010) Authigenic carbonates in upper Miocene sediments of the Tertiary Piedmont Basin (NW Italy): vestiges of an ancient gas hydrate stability zone? Geol Soc Am Bull 122(7/8):994–1010

Deng Y, Chen F, Hu Y et al (2020) Methane seepage patterns during the middle Pleistocene inferred from molybdenum enrichments of seep carbonates in the South China Sea. Ore Geol Rev 125:103701. https://doi.org/10.1016/j.oregeorev.2020.103701

Denison RE, Koepnick RB, Fletcher A et al (1994) Criteria for the retention of original seawater $^{87}Sr/^{86}Sr$ in ancient shelf limestones. Chem Geol 112(1/2):131–143

Dulski P (1994) Interferences of oxide, hydroxide and chloride analyte species in the determination of rare earth elements in geological samples by inductively coupled plasma-mass spectrometry. J Anal Chem 350:194–203

Elderfield H (1988) The oceanic chemistry of the rare-earth elements. Phil Trans Roy Soc Lond A 325:105–126

Elvert M, Hopmans EC, Treude T et al (2005) Spatial variations of menthanotrophic consortia at cold methane seeps: implications from a high-resolution molecular and isotopic approach. Geobiology 3:195–209

Ettwig KF, Butler MK, Le Pasilier D et al (2010) Nitrite-driven anaerobic methane oxidation by oxygenic bacteria. Nature 464:543–548

Feng D, Chen D (2015) Authigenic carbonates from an active cold seep of the northern South China Sea: new insights into fluid sources and past seepage activity. Deep-Sea Res II 122:74–83

Feng D, Chen D, Roberts HH (2009a) Petrographic and geochemical characterization of seep carbonate from Bush Hill (GC 185) gas vent and hydrate site of the Gulf of Mexico. Mar Pet Geol 26(7):1190–1198

Feng D, Chen D, Peckmann J (2009b) Rare earth elements in seep carbonates as tracers of variable redox conditions at ancient hydrocarbon seeps. Terra Nova 21(1):49–56

Feng D, Chen D, Peckmann J et al (2010) Authigenic carbonates from methane seeps of the northern Congo fan: microbial formation mechanism. Mar Pet Geol 27(4):748–756

Feng D, Lin Z, Bian Y et al (2013) Rare earth elements of seep carbonates: indication for redox variations and microbiological processes at modern seep sites. J Asian Earth Sci 65:27–33

Ferry JG (1992) Methane from acetate. J Bacteriol 174(17):5489–5495

Finch AA, Allison N (2007) Coordination of Sr and Mg in calcite and aragonite. Mineral Mag 71(5):539–552

Freslon N, Bayon G, Toucanne S et al (2014) Rare earth elements and neodymium isotopes in sedimentary organic matter. Geochim Cosmochim Acta 140:177–198

Gao Y (2019) Clumped isotope paleothermometry of authigenic carbonates from Late Cretaceous (Campanian) methane seeps in the Western Interior Seaway, South Dakota, USA. Thesis, Stony Brook University

Gao Y, Henkes GA, Cochran JK et al (2021) Temperatures of Late Cretaceous (Campanian) methane-derived authigenic carbonates from the Western Interior Seaway, South Dakota, USA, using clumped isotopes. Geol Soc Am Bull 133(11/12):2524–2534. https://doi.org/10.1130/B35846.1

Ge l, Chen W, Zhu B, Fan M, Yang T, Jiang S (2020) Sr and Nd isotopes of cold seep carbonates from the northern South China sea as proxies for fluid sources. Mar Pet Geol 115:104284

Ge L, Jiang S-Y, Swennen R et al (2010) Chemical environment of cold seep carbonate formation on the northern continental slope of South China Sea: evidence from trace and rare earth element geochemistry. Mar Geol 277(1−4):21–30

German CR, Elderfield H (1990) Application of the Ce anomaly as a paleoredox indicator: the ground rules. Paleoceanographica 5(5):823–833

Greinert J, Bohrmann G, Suess E (2001) Gas hydrate-associated carbonates and methane-venting at Hydrate Ridge: classification, distribution, and origin of authigenic lithologies. In: Paull CK, Dillon PW (eds) Natural gas hydrates: occurrence, distribution, and detection. American Geophysical Union, Washington, DC, pp 99–113

Greinert J, Bohrmann G, Elvert M (2002) Stromatolitic fabric of authigenic carbonate crusts: result of anaerobic methane oxidation at cold seeps in 4,850 m water depth. Int J Earth Sci 91(4):698–711

Grossman EL, Ku T-L (1986) Carbon and oxygen isotopic fractionation in biogenic aragonite: temperature effects. Chem Geol 59:59–74

Hagemann A, Leefmann T, Peckmann J et al (2012) Biomarkers from individual carbonate phases of an Oligocene cold-seep deposit. Lethaia 46(1):7–18. https://doi.org/10.1111/j.1502-3931.2012.00316.x

Haley BA, Klinkhammer GP, McManus J (2004) Rare earth elements in pore waters of marine sediments. Geochim Cosmochim Acta 68(6):1265–1279

Hall JLO, Newton RJ, Witts JD et al (2018) High benthic methane flux in low sulfate oceans: evidence from carbon isotopes in Late Cretaceous Antarctic bivalves. Earth Planet Sci Lett 497:113–122

Han X, Suess E, Sahling H et al (2004) Fluid activity on the Costa Rica margin: new results from authigenic carbonates. Int J Earth Sci 93:596–611

Handle KC (2014) Paleoecology of Late Cretaceous methane cold seeps of the Pierre Shale, South Dakota. Dissertation, City University of New York

Hein JR, Zierenberg RA, Maynard JB et al (2007) Barite-forming environments along a rifted continental margin, southern California borderland. Deep-Sea Res II 54:1327–1349

Hellebrandt SE, Hofmann S, Jordan N et al (2016) Incorporation of Eu(III) into calcite under recrystallization conditions. Sci Rep 6:33137. https://doi.org/10.1038/srep33137

Henkes GA, Passey BH, Wanamaker AD et al (2013) Carbonate clumped isotope compositions of modern marine mollusk and brachiopod shells: Geochim Cosmochim Acta 106:307–325

Himmler T, Bach W, Bohrmann G et al (2010) Rare earth elements in authigenic methane-seep carbonates as tracers for fluid composition during early diagenesis. Chem Geol 277(1/2):126–136

Himmler T, Haley BA, Torres ME et al (2013) Rare earth element geochemistry in cold-seep pore waters of Hydrate Ridge, northeast Pacific Ocean. Geo-Mar Lett 33(5):369–379

Himmler T, Smrzka D, Zwicker J et al (2018) Stromatolites below the photic zone in the northern Arabian Sea formed by calcifying chemotrophic microbial mats. Geology 46(4):339–342

Hryniewicz K (this volume-a) Ancient seep carbonates: from outcrop appearance to microscopic petrography. In: Kaim A, Cochran JK, Landman NH (eds) Ancient hydrocarbon seeps. Topics in geobiology, vol 50. Springer, New York

Hryniewicz K (this volume-b) Seeps around the world. In: Kaim A, Cochran JK, Landman NH (eds) Ancient hydrocarbon seeps. Topics in geobiology, vol 50. Springer, New York

Hu Y, Feng D, Peckmann J et al (2014) New insights into cerium anomalies and mechanisms of trace metal enrichment in authigenic carbonate from hydrocarbon seeps. Chem Geol 381:55–66

Hu Y, Feng D, Peckmann J et al (2020) The impact of diffusive transport of methane on pore-water and sediment geochemistry constrained by authigenic enrichments of carbon, sulfur, and trace

elements: a case study from the Shenhu area of the South China Sea. Chem Geol 553:119805. https://doi.org/10.1016/j.chemgeo.2020.119805

Hudson JD, Anderson TF (1989) Ocean temperatures and isotopic compositions through time. Trans R Soc Edinb Earth Sci 80:183–192

Jakubowicz M, Dopieralska J, Belka Z (2015a) Tracing the composition and origin of fluids at an ancient hydrocarbon seep (Holland Mound, Middle Devonian, Morocco): a Nd, REE and stable isotope study. Geochim Cosmochim Acta 156:50–74

Jakubowicz M, Berkpwski B, Correa ML et al (2015b) Stable Isotope Signatures of Middle Palaeozoic ahermatypic rugose corals—deciphering secondary alteration, vital fractionation effects, and palaeoecological implications. PLoS One 10(9):e0136289. https://doi.org/10.1371/journal.pone.0136289

Jakubowicz M, Dopieralska J, Kaim A et al (2019) Nd isotope composition of seep carbonates: towards a new approach for constraining subseafloor fluid circulation at hydrocarbon seeps. Chem Geol 503:40–51

Jakubowicz M, Kiel S, Goedert JL et al (2020) Fluid expulsion system and tectonic architecture of the incipient Cascadia convergent margin as revealed by Nd, Sr and stable isotope composition of mid-Eocene methane seep carbonates. Chem Geol 558:119872. https://doi.org/10.1016/j.chemgeo.2020.119872

Jakubowicz M, Agirrezabala LM, Dopieralska J et al (2021) The role of magmatism in hydrocarbon generation in sedimented rifts: a Nd isotope perspective from mid-Cretaceous methane-seep deposits of the Basque-Cantabrian Basin, Spain. Geochim Cosmochim Acta 393:223–248

Jenkins RG, Kaim A, Hikida Y et al (2007) Methane-flux-dependent lateral faunal changes in a Late Cretaceous chemosymbiotic assemblage from the Nakagawa area of Hokkaido, Japan. Geobiology 6:127–139

Jørgensen BB, Nelson DC (2004) Sulfide oxidation in marine sediments: geochemistry meets microbiology. In: Amend JP, Edwards KJ, Lyons TW (eds) Sulfur biogeochemistry—past and present, Geological Society of America Special Paper 379. Geological Society of America, Boulder, pp 63–81

Joseph C, Torres ME, Martin RA et al (2012) Using the $^{87}Sr/^{86}Sr$ of modern and paleoseep carbonates from northern Cascadia to link modern fluid flow to the past. Chem Geol 334:122–130

Joseph C, Campbell KA, Torres ME et al (2013) Methane-derived authigenic carbonates from modern and paleoseeps on the Cascadia margin: mechanisms of formation and diagenetic signals. Palaeogeogr Palaeoclimatol Palaeoecol 390:52–67

Joye S (2012) A piece of the methane puzzle. Nature 491:538–539

Kaplan IR, Rittenberg SC (1964) Microbiological fractionation of sulphur isotopes. J Gen Microbiol 34:195–212

Kelly SRA, Ditchfield PW, Doubleday PA et al (1995) An Upper Jurassic methane-seep limestone from the Fossil Bluff Group fore-arc basin of Alexander Island, Antarctica. J Sediment Res A 65(2):274–282

Kennedy M, Mrofka D, von der Borch C (2008) Snowball Earth termination by destabilization of equatorial permafrost methane clathrate. Nature 453:642–645

Kiel S (2015) Did shifting seawater sulfate concentrations drive the evolution of methane-seep ecosystems? Proc R Soc B 282(1804):20142908. https://doi.org/10.1098/rspb.2014.2908

Kiel S, Hansen C, Nitzsche KN et al (2014) Using $^{87}Sr/^{86}Sr$ ratios to date fossil methane seep deposits: methodological requirements and an example from the Great Valley Group, California. J Geol 122(4):353–366

Kim S, O'Neil JR (1997) Equilibrium and nonequilibrium oxygen isotope effects in synthetic carbonates. Geochim Cosmochim Acta 61:3461–3475. https://doi.org/10.1016/S0016-7037(97)00169-5

Kim J-H, Torres ME, Haley BA et al (2012) The effect of diagenesis and fluid migration on rare earth element distribution in pore fluids of the northern Cascadia accretionary margin. Chem Geol 291:152–165

Knittel K, Boetius A (2009) Anaerobic oxidation of methane: progress with an unknown process. Annu Rev Microbiol 63:311–334

Krause FF, Clark J, Sayegh SG et al (2009) Tube worm fossils or relic methane expulsing conduits? Palaios 24:41–50

Lacan F, Tachikawa K, Jeandel C (2012) Neodymium isotope composition of the oceans: a compilation of seawater data. Chem Geol 300(301):177–184

Lakshtanov LZ, Stipp SLS (2004) Experimental study of europium (III) coprecipitation with calcite. Geochim Cosmochim Acta 68(4):819–827

Landman NH, Cochran JK, Larson NL et al (2012) Methane seeps as ammonite habitats in the U.S. Western Interior Seaway revealed by isotopic analyses of well-preserved shell material. Geology 40(6):507–510. https://doi.org/10.1130/G32782.1

Landman NH, Cochran JK, Slovacek M et al (2018) Isotope sclerochronology of ammonites (*Baculites compressus*) from methane seep and non-seep sites in the Late Cretaceous Western Interior Seaway, USA: implications for ammonite habitat and mode of life. Am J Sci 318:603–639

Landman NH, Cochran JK, Brezina J et al (this volume) Methane seeps in the Late Cretaceous Western Interior Seaway. In: Kaim A, Cochran JK, Landman NH (eds) Ancient hydrocarbon seeps. Topics in geobiology, vol. 50, Springer, New York

Lietard C, Pierre C (2009) Isotopic signatures ($\delta^{18}O$ and $\delta^{13}C$) in bivalve shells from cold seeps and hydrothermal vents. Geobios 42:209–219

Lin Z, Sun X, Peckmann J et al (2016) How sulfate-driven anaerobic oxidation of methane affects the sulfur isotopic composition of pyrite: a SIMS study from the South China Sea. Chem Geol 440:26–41

Lin Z, Sun X, Strauss H et al (2017a) Multiple sulfur isotope constraints on sulfate-driven anaerobic oxidation of methane: evidence from authigenic pyrite in seepage areas of the South China Sea. Geochim Cosmochim Acta 211:153–173

Lin Z, Sun X, Lu Y et al (2017b) The enrichment of heavy iron isotopes in authigenic pyrite as a possible indicator of sulfate-driven anaerobic oxidation of methane: insights from the South China Sea. Chem Geol 449:15–29

Little CTS, Birgel D, Boyce AJ et al (2015) Late Cretaceous (Maastrichtian) shallow water hydrocarbon seeps from Snow Hill and Seymour Islands, James Ross Basin, Antarctica. Palaeogeogr Palaeoclimatol Palaeoecol 418:213–228

Loyd SJ, Sample J, Tripati RE et al (2016) Methane seep carbonates yield clumped isotope signatures out of equilibrium with formation temperatures. Nat Commun 7:12274

Luff R, Wallmann K (2003) Fluid flow, methane fluxes carbonate precipitation and biogeochemical turnover in gas hydrate-bearing sediments at Hydrate Ridge, Cascadia Margin: numerical modeling and mass balances. Geochim Cosmochim Acta 67(18):3404–3421

Luff R, Wallmann K, Aloisi G (2004) Numerical modeling of carbonate crust formation at cold vent sites: significance for fluid and methane budgets and chemosynthetic biological communities. Earth Planet Sci Lett 221:337–353

Machel HG (2000) Application of cathodoluminescence to carbonate diagenesis. In: Pagel M, Barbin V, Blanc P et al (eds) Cathodoluminescence in geosciences. Springer, New York, pp 271–301

MacRae ND, Nesbitt HW, Kronberg BI (1992) Development of a positive Eu anomaly during diagenesis. Earth Planet Sci Lett 109(3/4):585–591

Matsumoto R (2001) Methane hydrates. In: Steele JH, Thorpe SA, Turekian KK (eds) Encyclopedia of ocean sciences, 1st edn. Elsevier, New York, pp 1745–1757

Matveeva T, Savvichev AD, Semenova A et al (2015) Source, origin and spatial distribution of shallow sediment methane in the Chukchi Sea. Oceanography 28(3):202–217

Mazzini A, Ivanov MK, Parnell J et al (2004) Methane-related authigenic carbonates from the Black Sea: geochemical characterisation and relation to seeping fluids. Mar Geol 212:153–181

McArthur JM, Kennedy WJ, Chen M et al (1994) Strontium isotope stratigraphy for Late Cretaceous time: direct numerical calibration of the Sr isotope curve based on the US Western Interior. Palaeogeogr Palaeoclimatol Palaeoecol 108:95–119

McConnaughey TA (1989) ^{13}C and ^{18}O isotopic disequilibria in biological carbonates: I, patterns. Geochim Cosmochim Acta 53:151−162

McConnaughey TA, Gillikin DP (2008) Carbon isotopes in mollusk shell carbonates. Geo-Mar Lett 28:287–299
McLennan SM (1989) Rare-earth elements in sedimentary rocks—influence of provenance and sedimentary processes. Rev Mineral 21:169–200
Michaelis W, Seifert R, Nauhaus K et al (2002) Microbial reefs in the Black Sea fueled by anaerobic oxidation of methane. Science 297:1013–1015
Milucka J, Ferdelman TG, Polerecky L et al (2012) Zero-valent sulphur is a key intermediate in marine methane oxidation. Nature 491:541–546
Miyajima Y, Jenkins RG (this volume) Biomarkers in ancient hydrocarbon-seep carbonates. In: Kaim A, Cochran JK, Landman NH (eds) Ancient hydrocarbon seeps. Topics in geobiology, vol 50. Springer, New York
Miyajima Y, Watanabe Y, Jenkins RG et al (2018) Diffusive methane seepage in ancient deposits: examples from the Neogene Shin'etsu sedimentary basin, central Japan. J Sediment Res 88:449–466
Naehr TH, Eichhubl P, Orphan VJ et al (2007) Authigenic carbonate formation at hydrocarbon seeps in continental margin sediments: a comparative study. Deep-Sea Res II 54:1268–1291
Natalicchio M, Birgel D, Dela Pierre F et al (2012) Polyphasic carbonate precipitation in the shallow subsurface: insights from microbially-formed authigenic carbonate beds in the upper Miocene sediments of the Tertiary Piedmont (NW Italy). Palaeogeogr Palaeoclimatol Palaeoecol 329(330):158–172
Nothdurft LD, Webb GE, Kamber BS (2004) Rare earth element geochemistry of Late Devonian reefal carbonates, Canning Basin, Western Australia: confirmation of a seawater REE proxy in ancient limestones. Geochim Cosmochim Acta 68(2):263–283
Nöthen K, Kasten S (2011) Reconstructing changes in seep activity by means of pore water and solid phase Sr/Ca and Mg/Ca ratios in pockmark sediments of the Northern Congo Fan. Mar Geol 287(1−4):1–13
Paull CK, Ussler W III, Holbrook WS et al (2008) Origin of pockmarks and chimney structures on the flanks of the Storegga Slide, offshore Norway. Geo-Mar Lett 28:43–51
Peckmann J, Thiel V (2004) Carbon cycling at ancient methane-seeps. Chem Geol 205:443–467
Peckmann J, Thiel V, Michaelis W et al (1999) Cold seep deposits of Beauvoisin (Oxfordian, southeastern France) and Marmorito (Miocene, northern Italy): microbially induced authigenic carbonates. Int J Earth Sci 88:60–75
Peckmann J, Reimer A, Luth U et al (2001) Methane-derived carbonates and authigenic pyrite from the northwestern Black Sea. Mar Geol 177:129–150
Peckmann J, Goedert JL, Thiel V et al (2002) A comprehensive approach to the study of methane-seep deposits from the Lincoln Creek Formation, western Washington State, USA. Sedimentology 49:855–873
Peckmann J, Goedert JL, Heinrichs T et al (2003) The Late Eocene 'Whiskey Creek' methane-seep deposit (western Washington State) part II: petrology, stable isotopes, and biogeochemistry. Facies 48:241–254
Peckmann J, Thiel V, Reitner J et al (2004) A microbial mat of a large sulfur bacterium preserved in a Miocene methane-seep limestone. Geomicrobiol J 21:247–255. https://doi.org/10.1080/01490450490438757
Peckmann J, Campbell KA, Walliser OH et al (2007) A Late Devonian hydrocarbon-seep deposit dominated by dimerelloid brachiopods, Morocco. Palaios 22(2):114–122
Peketi A, Mazumdar A, Joshi RK et al (2012) Tracing the paleo sulfate-methane transition zones and H_2S seepage events in marine sediments: an application of C-S-Mo systematics. Geochem Geophys Geosyst 13(10):Q10007. https://doi.org/10.1029/2012GC004288
Pichler T, Veizer J (2004) The precipitation of aragonite from shallow-water hydrothermal fluids in a coral reef, Tutum Bay, Ambitle Island, Papua New Guinea. Chem Geol 207(1/2):31–45
Pierre C, Blanc-Valleron M-M, Caquineau S et al (2014) Mineralogical, geochemical and isotopic characterization of authigenic carbonates from the methane-bearing sediments of the Bering Sea continental margin (IODP Expedition 323, Sites U1343−U1345). Deep-Sea Res II 125(126):133–144

Planavsky NJ, Bekker A, Hofmann A et al (2012) Sulfur record of rising and falling marine oxygen and sulfate levels during the Lomagundi event. PNAS 109(45):18300–18305
Popp BN, Anderson TF, Sandberg PA (1986) Textural, elemental, and isotopic variations among constituents in Middle Devonian limestones, North America. J Sediment Petrol 56(5):715–727
Pourret O, Davranche M, Gruau G et al (2008) New insights into cerium anomalies in organic-rich alkaline waters. Chem Geol 251(1−4):120–127
Preisler A, de Beer D, Lichtschlag A et al (2007) Biological and chemical sulfide oxidation in a *Beggiatoa* inhabited marine sediment. ISME J 1:341–353. https://doi.org/10.1038/ismej.2007.50
Reeder RJ (1983) Crystal chemistry of the rhombohedral carbonates In: Reeder RJ (ed) Carbonates: mineralogy and chemistry. Reviews in Mineralogy vol 11. Mineralogical Society of America, Chantilly, pp 1−47
Reitner J, Peckmann J, Blumenberg M et al (2005) Concretionary methane-seep carbonates and associated microbial communities in Black Sea sediments. Palaeogeogr Palaeoclimatol Palaeoecol 227:18030
Ritger S, Carson B, Suess E (1987) Methane-derived authigenic carbonates formed by subduction-induced pore-water expulsion along the Oregon/Washington margin. Geol Soc Am Bull 98:147–156
Roberts HH, Feng D, Joye SB (2010) Cold-seep carbonates of the middle and lower continental slope, northern Gulf of Mexico. Deep-Sea Res II 57:2040–2054
Rongemaille E, Bayon G, Pierre C et al (2011) Rare earth elements in cold seep carbonates from the Niger Delta. Chem Geol 286:196–206
Rowe A, Landman NH, Cochran JK et al (2020) Late Cretaceous methane seeps as habitats for newly hatched ammonites. Palaios 35:1–13
Sample JC, Reid MR, Tobin HJ et al (1993) Carbonate cements indicate channeled fluid flow along a zone of vertical faults at the deformation front of the Cascadia accretionary wedge (northwest U.S. coast). Geology 21:507–510
Sansone FJ, Martens CS (1981) Methane production from acetate and associated methane fluxes from anoxic coastal sediments. Science 211:707–709
Savard MM, Beauchamp B, Veizer J (1996) Significance of aragonite cements around Cretaceous methane seeps. J Sediment Res 66(3):430–438
Sayama M (2001) Presence of nitrate-accumulating sulfur bacteria and their influence on nitrogen cycling in a shallow coastal marine sediment. Appl Environ Microbiol 67(8):3481–3487. https://doi.org/10.1128/AEM.67.8.3481-3487.2001
Schwedt A, Kreutzmann A-C, Polerecky L et al (2012) Sulfur respiration in a marine chemolithotrophic *Beggiatoa* strain. Front Microbiol 2:276. https://doi.org/10.3389/fmicb.2011.00276
Shackleton NJ, Kennett JP (1975) Paleotemperature history of the Cenozoic and initiation of Antarctic glaciation: oxygen and carbon isotope analyses in DSDP sites 277, 279 and 281. Deep Sea Drilling Project Initial Rep 29:743–755
Shields GA, Deynoux M, Strauss H et al (2007) Barite-bearing cap dolostones of the Taoudeni Basin, northwest Africa: sedimentary and isotopic evidence for methane seepage after a Neoproterozoic glaciation. Precambrian Res 153:209–235
Sholkovitz ER, Piepgras DJ, Jacobsen SB (1989) The pore water chemistry of rare earth elements in Buzzards Bay sediments. Geochim Cosmochim Acta 53:2847–2856
Smrzka D, Zwicker J, Klügel A et al (2016) Establishing criteria to distinguish oil-seep from methane-seep carbonates. Geology 44(8):667–670
Smrzka D, Zwicker J, Kolonic S et al (2017) Methane seepage in a Cretaceous greenhouse world recorded by an unusual carbonate deposit from the Tarfaya Basin, Morocco. Depositional Rec 3(1):4–37
Smrzka D, Zwicker J, Misch D et al (2019) Oil seepage and carbonate formation: a case study from the southern Gulf of Mexico. Sedimentology 66(6):2318–2353
Smrzka D, Feng D, Himmler T et al (2020) Trace elements in methane-seep carbonates: potentials, limitations, and perspectives. Earth Sci Rev 208:103263. https://doi.org/10.1016/j.earscirev.2020.103263

Soyol-Erdene T-O, Huh Y (2013) Rare earth element cycling in the pore waters of the Bering Sea Slope (IODP Exp. 323). Chem Geol 358:75–89

Stakes DS, Orange D, Paduan JB et al (1999) Cold-seeps and authigenic carbonate formation in Monterey Bay, California. Mar Geol 159:93–109

Stipp SLS, Lakshtanov LZ, Jensen JT et al (2003) Eu^{3+} uptake by calcite: preliminary results from coprecipitation experiments and observations with surface-sensitive techniques. J Contam Hydrol 61(1−4):33–43

Sverjensky DA (1984) Europium redox equilibria in aqueous solution. Earth Planet Sci Lett 67(1):70–78

Tachikawa K, Arsouze T, Bayon G et al (2017) The large-scale evolution of neodymium isotopic composition in the global modern and Holocene ocean revealed from seawater and archive data. Chem Geol 457:131–148

Teichert BAM, Bohrmann G, Suess E (2005) Chemoherms on Hydrate Ridge—unique microbially-mediated carbonate build-ups growing into to the water column. Palaeogeogr Palaeoclimatol Palaeoecol 227:67–85

Tong H, Feng D, Peckmann J et al (2019) Environments favoring dolomite formation at cold seeps: a case study from the Gulf of Mexico. Chem Geol 518:9–18

Torres ME, McManus JW, Huh C-A (2002) Fluid seepage along the San Clemente Fault scarp: basin-wide impact on barium cycling. Earth Planet Sci Lett 203:181–194

Tostevin R, Shields GA, Tarbuck GM et al (2016) Effective use of cerium anomalies as a redox proxy in carbonate-dominated marine settings. Chem Geol 438:146–162

Tribovillard N, Armynot du Châtelet E, Gay A et al (2013) Geochemistry of cold seepage-impacted sediments: per-ascensum or per-descensum trace metal enrichment? Chem Geol 340:1–12

Tucker ME, Wright VP (1990) Carbonate sedimentology. Blackwell Scientific, Oxford

Walker RJ, Hanson GN, Papike JJ et al (1986) Nd, O and Sr isotopic constraints on the origin of Precambrian rocks, southern Black Hills, South Dakota. Geochim Cosmochim Acta 50:2833–2846

Wang S, Yan W, Chen Z et al (2014) Rare earth elements in cold seep carbonates from the southwestern Dongsha area, northern South China Sea. Mar Pet Geol 57:482–493

Wang Q, Tong H, Huang C-Y et al (2018) Tracing fluid sources and formation conditions of Miocene hydrocarbon-seep carbonates in the central Western Foothills, central Taiwan. J Asian Earth Sci 168:186–196

Wang Q, Chen D, Peckmann J (2019) Iron shuttle controls on molybdenum, arsenic, and antimony enrichment in Pliocene methane-seep carbonates from the southern Western Foothills, southwestern Taiwan. Mar Pet Geol 100:263–269

Webb GE, Nothdurft LD, Kamber BS et al (2009) Rare earth element geochemistry of scleractinian coral skeleton during meteoric diagenesis: a sequence through neomorphism of aragonite to calcite. Sedimentology 56(5):1433–1463

Whiticar MJ (1999) Carbon and hydrogen isotope systematics of bacterial formation and oxidation of methane. Chem Geol 161:291–314

Wiese F, Kiel S, Pacvk A et al (2015) The beast burrowed, the fluid followed—crustacean burrows as methane conduits. Mar Pet Geol 66:631–640

Williscroft K, Grasby SE, Beauchamp B et al (2017) Extensive Early Cretaceous (Albian) methane seepage on Ellef Ringnes Island, Canadian High Arctic. Geol Soc Am Bull 129(7/8):788–805

Zhang N, Lin M, Snyder GT et al (2019) Clumped isotope signatures of methane-derived authigenic carbonate presenting equilibrium values of their formation temperatures. Earth Planet Sci Lett 512:207–213

Zwicker J, Smrzka D, Gier S et al (2015) Mineralized conduits are part of the uppermost plumbing system of Oligocene methane-seep deposits, Washington Stare (USA). Mar Pet Geol 66:616–630

Zwicker J, Smrzka D, Himmler T et al (2018) Rare earth elements as tracers for microbial activity and early diagenesis: a new perspective from carbonate cements of ancient methane-seep deposits. Chem Geol 501:77–85